Journal of Nanobiotechnology

RESEARCH

Open Access

Role of bioactive magnetic nanoparticles in the prevention of wound pathogenic biofilm formation using smart nanocomposites

Naeimeh Eghbalifam[1], Seyed Abbas Shojaosadati[1*] and Sameereh Hashemi-Najafabadi[2]

Abstract

Background Biofilm formation and its resistance to various antibiotics is a serious health problem in the treatment of wound infections. An ideal wound dressing should have characteristics such as protection of wound from microbial infection, suitable porosity (to absorb wound exudates), proper permeability (to maintain wound moisture), non-toxicity, and biocompatibility. Although silver nanoparticles (AgNPs) have been investigated as antimicrobial agents, their limitations in penetrating into the biofilm, affecting their efficiency, have consistently been an area for further research.

Results Consequently, in this study, the optimal amounts of natural and synthetic polymers combination, along with AgNPs, accompanied by iron oxide nanoparticles (IONPs), were utilized to fabricate a smart bionanocomposite that meets all the requirements of an ideal wound dressing. Superparamagnetic IONPs (with the average size of 11.8 nm) were synthesized through co-precipitation method using oleic acid to improve their stability. It was found that the addition of IONPs to bionanocomposites had a synergistic effect on their antibacterial and antibiofilm properties. Cytotoxicity assay results showed that nanoparticles does not considerably affect eukaryotic cells compared to prokaryotic cells. Based on the images obtained by confocal laser scanning microscopy (CLSM), significant AgNPs release was observed when an external magnetic field (EMF) was applied to the bionanocomposites loaded with IONPs, which increased the antibacterial activity and inhibited the formation of biofilm significantly.

Conclusion These finding indicated that the nanocomposite recommended can have an efficient properties for the management of wounds through prevention and treatment of antibiotic-resistant biofilm.

Keywords Electrospinning, Iron oxide nanoparticles, Pathogenic biofilm inhibition, Silver nanoparticles, Smart nanocomposites, Wound dressing

*Correspondence:
Seyed Abbas Shojaosadati
Shoja_sa@modares.ac.ir
Full list of author information is available at the end of the article

Graphical Abstract

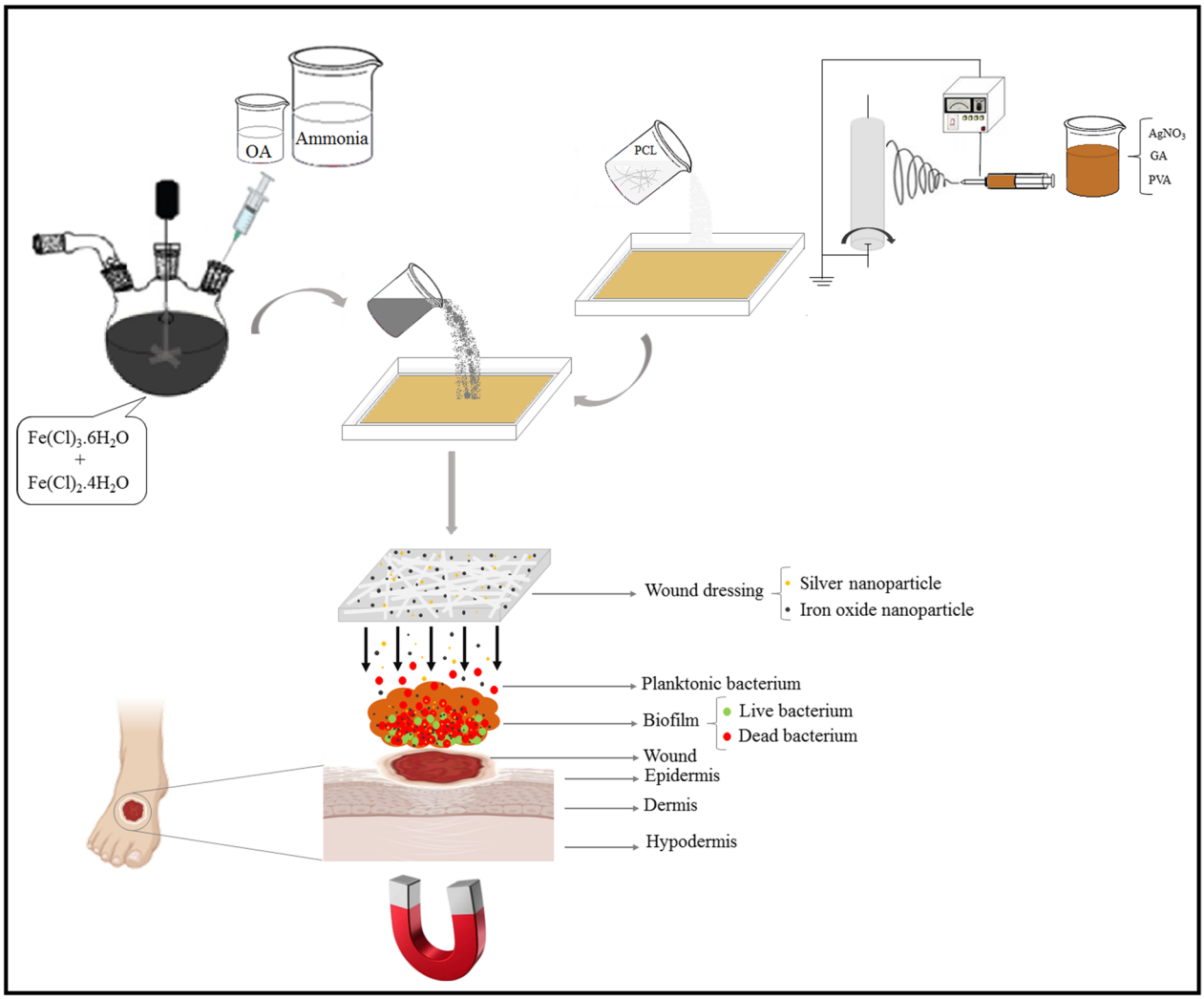

Introduction

Bacterial infections, as a serious health problem, are among the leading causes of death, especially in skin wound treatment [1–3]. It has been shown that antimicrobial therapy fails due to the increased bacterial resistance to various antibiotics [4–6]. In chronic infections, complete inhibition of bacterial growth via antibiotics is not possible since the growth state changes from planktonic to biofilm [7–13]. Biofilm is a community of microorganisms attached to a particular surface and is embedded in a self-made extracellular polymeric substance (EPS) [9, 12, 14–16]. The EPS matrix reduces the penetration of antibiotics to reach the microorganisms within the biofilm. This is why biofilms are highly resistant to most antibiotics (up to 1000 times more than planktonic cells) [8, 10]. Additionally, since the polymer matrix keeps the nutrients, biofilms are more likely to survive, and this is the reason antibiotics are not able to destroy the biofilm cells [17]. Therefore, biofilm formation is one of the most common challenges in the wound healing process, affecting the treatment time, cost, and failure rate [18, 19]. Thus, it is necessary to develop new approaches to inhibit biofilm formation, treat bacterial infections, and be less toxic to patients.[20, 21].

The strong antibacterial activity of the AgNPs makes them attractive agents for preventing the evolution of antibiotic resistance. They can attack different sites of the cells which are vital to physiological functions (e.g.,

the cell wall, DNA/RNA synthesis, and electron transport) [12, 22–24]. However, these nanoparticles have some drawbacks including cytotoxicity [10, 24, 25], easy oxidation [12, 26], aggregation [7, 24, 27], and limited penetration into tissues and biofilms [28, 29].

Some solutions have been introduced to overcome these issues. For instance, integration of AgNPs with biopolymers can prevent them from aggregation and oxidation [30]. In addition, biopolymers can provide other benefits such as the ability to absorb wound exudates, non-toxicity, and biocompatibility, which are essential qualities of an ideal wound dressing [5]. Among biopolymers, gums have a high absorbance capacity, which makes them promising materials for this application [31, 32]. Gum Arabic (GA) is an inexpensive material that possesses interesting properties, such as hydrophilicity, biocompatibility, and biodegradability. It can be used in the green synthesis of AgNPs with no additional reducing agents [32]. Moreover, polyvinyl alcohol (PVA) is a synthetic, hydrophilic, and non-toxic polymer with excellent wound dressing properties that can improve gum Arabic's electrospinability.

On the other hand, polycaprolacton (PCL) is a synthetic biodegradable polyester that has suitable mechanical properties and can be applied to biomedical applications. It increases the structural strength of composites in humid environments.

The problem of low penetration and consequently poor antibacterial efficacy of AgNPs against biofilm infections can be compensated by IONPs since they are responsive to EMF [33, 34]. In particular, magnetite nanoparticles (Fe_3O_4) are among the most popular nanoparticles in biomedical applications due to their unique properties, including superparamagnetism and biocompatibility [6, 35, 36]. Therefore, these binary systems combine the benefits of both nanoparticle types, and by integrating silver and iron oxide nanoparticles in polymers with optimum composition, a smart nanofiber composite can be synthesized that provides all the features an ideal wound dressing needs.

In our previous study, GA/PVA/PCL nanocomposites were prepared using a combination of the electrospinning and the coating methods, resulting in the optimum composition in the nanocomposite based on the porosity, water absorption, and water vapor permeability, but its effectiveness on inhibiting biofilm formation and increasing antibacterial activity was not explored. Consequently, the present study aims to develop a desirable fiber nanocomposite (containing silver and iron oxide nanoparticles) as a suitable wound dressing, that will provide a synergistic effect to inhibit the formation of antibiotic-resistant biofilms. The synthesized IONPs, characterized using TEM, DLS, XRD, FTIR, TGA, and VSM analyses, were added to silver-containing nanocomposites and their performance was evaluated through various assays. Nanocomposites with different concentrations of IONPs were investigated for their magnetic properties, and their antimicrobial activity was determined by measuring the radius of inhibition zone. Additionally, cytocompatibility was assessed by cytotoxicity and proliferation studies on mouse embryonic fibroblast cells. As a final step, the biofilm inhibitory abilities of the nanocomposites were evaluated against two common wound pathogen biofilm: *Staphylococcus aureus* and *Pseudomonas aeruginosa*.

Materials and methods

Materials

PVA, Mw: 85000–124000 g/mol, PCL, Mw: ~ 80000 g/mol and 3-(4,5-dimethylthiazol-2- yl)2,5-diphenyltetrazolium bromide (MTT) were purchased from Sigma-Aldrich (USA). GA, dimethylformamide (DMF, 99.80%), chloroform (99.00–99.40%), silver nitrate (99.80%), ferrous chloride tetrahydrate ($FeCl_2.4H_2O$), ferric chloride heptahydrate ($FeCl_3.7H_2O$), oleic acid, and ammonia solution (32%) were supplied from Merck (Germany). All chemicals and solvents were of analytical grade and used without any further purification. *Staphylococcus aureus* (IBRC-M 10917) and *Pseudomonas aeruginosa* (ATCC 27853) were obtained from the Iranian Biological Resource Center (IBRC) and the American Type Culture Collection (ATCC), respectively. Mouse embryonic fibroblast (MEF) cells (RSCB0182) were obtained from the Royan Institute (Iran) for Stem Cell Biology and Technology.

Samples preparation

Preparation of electrospinning solutions

Based on the optimal composition obtained in our previous study [32], 348 mg GA and 366 mg PVA were dissolved in deionized water (3 mL) and dimethylformamide (DMF, 3 mL, at 90 °C), respectively, under magnetic stirring until homogenous solutions were obtained. Then, silver nitrate was added to the GA solution. The concentration of silver nitrate in different nanocomposites were 0 (samples 1, 5, 9, and 13), 0.096% (samples 2, 6, 10, and 14), 0.96% (samples 3, 7, 11, and 15), and 1.92% (samples 4, 8, 12 and 16), respectively. In the process of dissolving the silver nitrate, AgNPs were synthesized, and the solution gradually darkened in color. GA-Ag + and PVA solutions were mixed overnight after the silver nitrate was completely dissolved.

Fabrication of GA/PVA/Ag fibrous nanocomposite

A 10 mL syringe was filled with the prepared solution, and the electrospinning process was used to produce nanofibers on an aluminum foil. All of the electrospinning parameters were chosen based on our previous research (feeding rate: 0.5 mL/h, applied voltage: 18 kV, tip-to-collector distance: 150 mm, rotation speed of collector: 500 rpm, electrospinning time: 12 h) [32].

Coating of the fibrous nanocomposite

186 mg PCL was dissolved in chloroform and the resultant nanocomposite from the last section was immersed in this solution, and then the solvent was evaporated with a lab oven (50 °C). After that, the PCL-coated sheet was peeled off from the aluminum foil [32].

Synthesis of IONPs coated with oleic acid

Oleic acid-coated Fe_3O_4 nanoparticles were synthesized by the chemical co-precipitation method. Oleic acid was used to improve the stability and consequently better performance of the IONPs. $FeCl_2{\cdot}4H_2O$ (199 mg) and $FeCl_3{\cdot}6H_2O$ (540 mg) as precursors were dissolved in 60 mL of deionized water (ambient temperature). The mixture was exposed to N_2 in a closed system to avoid ferrous ion oxidation. While stirring, 100 µL of oleic acid as the surfactant and 7 mL of ammonia solution (32%) were added to the reaction mixture immediately. The temperature was raised to 60 °C, and oleic acid was added twice more at 5-min intervals. After 30 min, IONPs were collected by the use of a magnet and then washed with water three times [37].

Preparation of Ag/IO nanocomposites

In order to fabricate Ag/IO nanocomposites, IONPs were added to the nanocomposites via an adsorption procedure. Desired concentrations of IONPs (based on the experimental design pre-tests data) were dispersed in isopropanol through ultrasonication (30 min). Afterward, the fibrous nanocomposites (containing different concentrations of the AgNPs, determined by the pre-tests of the experimental design) were immersed in the suspension for 1 h using an orbital shaker.

Experimental design

A full factorial design of experiments was used to explore the effects of two variables including the AgNPs' concentration (in 4 levels) and the IONPs' concentration (in 4 levels). All experiments were carried out in triplicate at least, and the results are expressed as: mean ± SD. Statistical analysis was performed using the one-way ANOVA followed by the Tukey HSD test for post hoc comparisons. P-values less than 0.05 ($p < 0.05$) were regarded as significant.

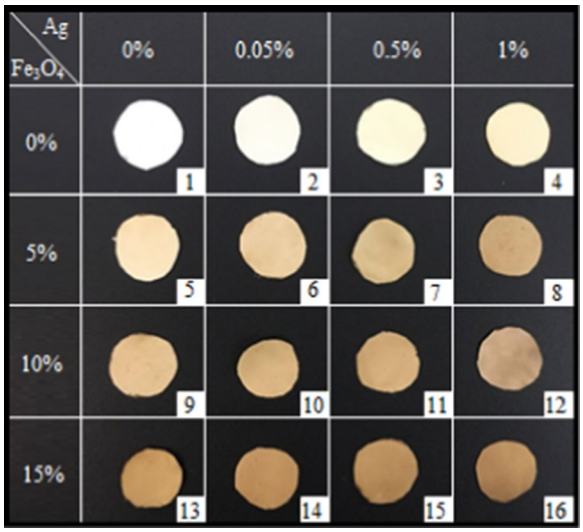

Fig. 1 The color of the nanocomposites with different concentrations of AgNPs (0, 0.05, 0.5, and 1%) and IONPs (0, 5, 10, and 15%), samples of 1–16

Levels of the variables

Based on the results of the pre-tests, the levels of each variable were determined (data not shown). Thus, 0, 0.05, 0.5, 1%, and 0, 5, 10, 15%, were chosen for the concentrations of the silver nanoparticles and the IONPs (16 samples).

The images of the prepared samples are given in Fig. 1. The color of the nanoparticles-free sample is white, but changes to yellow when AgNPs are added. The presence of the IONPs in the nanocomposites changes their color into brown. A higher nanoparticle concentration results in a darker sample color.

Evaluation of nanocomposite

The effects of the variables on the characteristics and the performance of the resultant nanocomposite were investigated in various ways as follows:

A. Antibacterial assay

Agar diffusion method

The antibacterial activity of the nanocomposites against *S. aureus*, *methicillin resistant Staphylococcus aureus (MRSA)*, *P. aeruginosa*, *E. coli* and *C. albicans* was evaluated using the agar diffusion test. The surface of each agar plate was inoculated by swabbing with 0.5 McFarland

turbidity standard microbial suspensions (0.5 McFarland turbidity standard provided optical density between 0.08 and 0.1 at 600 nm, roughly equivalent to 1.5×10^8 CFU/mL). Samples were placed on the surface of the inoculated plates. After 24 h incubation at 37 °C, the inhibition zone formed around each sample was measured in five directions, and the average diameter was determined [38].

Plate count method (colony forming efficiency)

The two bacteria (*S. aureus* and *P.* aeruginosa) were cultivated in 10 mL of the bacterial suspension in nutrient broth (0.5 McFarland concentration standard) and one piece of each nanocomposite (1 cm × 1 cm) was immersed in bacterial suspension in each tube. The tubes were incubated for 24 h at 37 °C. Then, 100 µL of the content of each tube was taken out and serially diluted (up to seven times) and spread on nutrient agar. The plates were incubated for 24 h at 37 °C. The number of bacterial colonies was counted and the average count of the three plates was determined. Finally, bacterial growth inhibition was calculated as follows:

$$\text{Bacterial growth inhibition}(\%) = \frac{(A-B)}{A} \times 100$$

where A & B are the numbers of bacterial colonies (CFU/mL) of control (sample 1) and sample plates, respectively.

B. Measurement of reactive oxygen species (ROS) generation

The ROS generation was determined according to the previously reported protocol using 2′,7′-dichlorofluorescein diacetate (DCFH-DA, Sigma, Germany, D6883) with slight modification [33, 39]. Bacterial cells (10^6 CFU/mL) were treated with the nanocomposites (1×1 cm^2) at 37 °C for 18 h. Then the growth media was removed and after addition of 2 mL PBS, cells were centrifuged at 1500 rpm for 5 min at 4 °C. The bacteria were collected and resuspended in 1 mL PBS and incubated with 2 µL DCFH-DA in darkness at 37 °C for 45 min. Then 1 mL PBS was added to each sample and they were centrifuged for 5 min at 1500 rpm to remove the residual DCFH-DA solution and the pellets were resuspended in 0.5 mL PBS. Finally, 3 µL of propidium iodide was added to each sample and the ROS production was analyzed using BD FACS Calibur flow cytometer (BD biosciences, San Jose, CA, USA). The bacteria in presence of nanoparticles-free nanocomposites were taken as control.

C. In vitro cytotoxicity

In vitro cytotoxicity effect of the nanocomposites was assessed with the 3-(4,5-dimethylthiazol-2-yl)-2,5-diphenyltetrazolium bromide (MTT) assay on the fibroblast and macrophage cells. Within each sample (1 cm^2), the MEF cells at a density of 10^4 cells/well were seeded in Dulbecco's modified Eagle's medium (DMEM)/high glucose supplemented with 15% fetal bovine serum (FBS) and 1% penicillin/streptomycin in a 48-well culture plate, and incubated in a humidified atmosphere, 5% CO_2 at 37 °C. The control well contained only the culture medium, without any nanocomposite (assuming 100% cell viability) [40]. Five replicates were performed to determine the cell viability of each sample at days 1, 3, 5, and 7 by the MTT assay. After each prearranged incubation time, 150 µL fresh medium containing the MTT solution was replaced with the old medium and the plate was incubated for 3 h at 37 °C to let the living cells produce formazan. After that, the medium including residual MTT was removed, dimethyl sulfoxide (DMSO) was added to each well, and 100 µL of the new medium was transferred to a 96-well plate. Finally, the optical density (OD) of the samples was measured by ELISA (enzyme-linked immunosorbent assay) reader at a wavelength of 570 nm. The cell viability percentage was determined by using the following equation [41]:

$$\textit{Cell viability}(\%) = \frac{Abs_{570}(\textit{Treated cells})}{Abs_{570}(\textit{Control cells})} \times 100$$

D. Biofilm inhibition

To evaluate the antibiofilm activity of the prepared samples, *Staphylococcus aureus* and *Pseudomonas aeruginosa* bacteria were used. The nanocomposites were sterilized with ethanol (99%) and placed in 96-well plates. Then, 180 µL sterile culture medium (nutrient broth) and 20 µL bacteria solution (10^6 CFU/mL) were added to the wells. Plates were incubated at 37 °C for 24 h to allow the formation of biofilms. The excessive medium was then slowly removed, and the wells were washed with autoclaved PBS and stained with 100 µL crystal violet (0.1%). After 15–30 min, the wells were rinsed again with autoclaved PBS three times and then dried. In the next step, 100 µL ethanol (99%) was added to each well to dissolve the adsorbed crystal violet by the biofilms. The same procedure was also used for the control wells, except for the omission of the nanocomposites. [42–44].

The optical density (OD) of the mixed solution was measured at 595 nm using ELISA reader. The biofilm Inhibition was calculated using the following equation:

$$Biofilm\ Inhibition(\%) = (\frac{OD_{Control} - OD_{sample}}{OD_{Control}}) \times 100\%$$

For visual inspection of the biofilm inhibition by the nanocomposites and the effect of the EMF application, Confocal Laser Scanning Microscopy (CLSM) was used. Sterile samples were placed in 12-well plates, and 1.5 mL of sterile culture medium (nutrient broth) and 0.5 mL of bacteria solution (1.5×10^8 CFU/mL) were added into the wells. Then, the plates were incubated at 37 °C for 48 h to form biofilm. After that, wells were rinsed three times with PBS, stained with SYTO9 (2 µM) and propidium iodide (PI) (4 µM) incubated for 15 min, and analyzed by CLSM (Zeiss LSM700). The wavelengths of 488 and 525 nm were used as excitation and emission wavelengths for the detection of SYTO9, respectively. Propidium iodide was excited at 520 nm, and its emission was measured at 620 nm. The wells without nanocomposite were considered to be the control groups [7, 33].

Characterization of the samples and their components

The morphology of IONPs was studied using a Philips EM 208S transmission electron microscopy (TEM). To prepare samples for TEM analysis, iron oxide nanoparticle solution was dropped on the cooper grid and dried at ambient temperature. Dynamic light scattering (DLS) analysis was performed using Particle Metrix GmbH (Germany) to determine the hydrodynamic diameter (D_H) and the particle size distribution of IONPs. X-ray diffraction (XRD) analysis was carried out using X'Pert MPD (Philips, Netherlands) with Co-kα radiation (where λ = 1.54056 Å and the Bragg's angel, 2θ, in the range of 5–80°). Fourier-transform infrared (FTIR) spectra were recorded using a Perkin–Elmer ATR–FTIR spectrometer spectrum 400. The wave number range and the resolution were 400–4000 cm^{-1}, and 2 cm^{-1}, respectively. Thermogravimetric analysis (TGA) and the corresponding derivative (dTGA) were performed using a Dupont 951 in the temperature range of 25–700 °C in an N_2 atmosphere to confirm the surface modification of IONPs by oleic acid. The magnetic properties of the IONPs and the nanocomposites were investigated using MDKFT (Danesh Pajouh Kashan Co., Iran) vibrating sample magnetometer (VSM) with a variation of the applied field between − 12000 and 12000 Oe at ambient temperature. To study the morphology and distribution of silver and iron oxide nanoparticles in the nanocomposites, field-emission scanning electron microscopy (MIRA 3, TESCAN, Czech Republic), energy-dispersive x-ray spectroscopy (EDX), and element map were used.

Results and discussion

IONPs characterization

Ammonia solution was added to the mixture of the iron salts (in bright yellow) and its color turned to black, resulting in the generation of iron (III) & iron (II) hydroxides because of the hydrolysis of Fe^{3+} and Fe^{2+}, respectively. In addition, iron (III) hydroxide was converted to another compound (FeOOH) that reacted with $Fe(OH)_2$ to produce Fe_3O_4. Fe^{2+} to Fe^{3+} molar ratio was 1:2 to obtain high efficiency in magnetite production and to prevent the oxidation of Fe^{2+} to Fe^{3+}. General reactions in the process of Fe_3O_4 formation are listed below (Eqs. (1–4)) [45].

$$Fe^{3+}(aq) + 3OH^{-}(aq) \rightarrow Fe(OH)_3(aq) \quad (1)$$

$$Fe(OH)_3(aq) \rightarrow FeOOH(aq) + H_2O(l) \quad (2)$$

$$Fe^{2+}(aq) + 2OH^{-}(aq) \rightarrow Fe(OH)_2(aq) \quad (3)$$

$$2FeOOH(aq) + Fe(OH)_2(aq) \rightarrow Fe_3O_4(s) + 2H_2O(l) \quad (4)$$

TEM images of oleic acid-coated magnetite nanoparticles are demonstrated in Fig. 2a, b. These images indicate that near-spherical nanoparticles with uniform size (approximately 10 nm) have been synthesized. It is also evident that the surface modification of nanoparticles with oleic acid did not meaningfully change the size of the nanoparticles. DLS analysis, which is based on the Brownian motion of the particles, provides quantitative results of the particle size and particle size distribution. Figure 2c illustrates a narrow size distribution in the range of 7.60–25.55 nm with an average of 11.8 nm, that is in good agreement with the TEM results.

Figure 3a indicates the X-ray diffractogram of IONPs. The XRD pattern of the nanoparticles exhibits peaks at 2Θ = 21.6, 35.3, 41.6, 50.7, 63.3, 67.5, and 74.5° which are attributed to (111), (220), (311), (400), (422), (511), and (440) planes, respectively. The results are in accordance with the magnetite (JCPDS 19–629) reference patterns [46, 47].

Figure 3b shows the FTIR spectrum of the modified IONPs. The characteristic bands at 444 and 590 cm^{-1} are assigned to Fe–O bonding [48]. Two characteristic bands at 1430 and 1524 cm^{-1} (due to stretching vibration of COO^{-}), confirm the presence of oleic acid on the nanoparticle surface [49]. Other characteristic absorption peaks at 2920 and 2850 cm^{-1} are related to the asymmetric and symmetric stretching of CH_2 in oleic acid structure, respectively. The bending vibration of the OH band

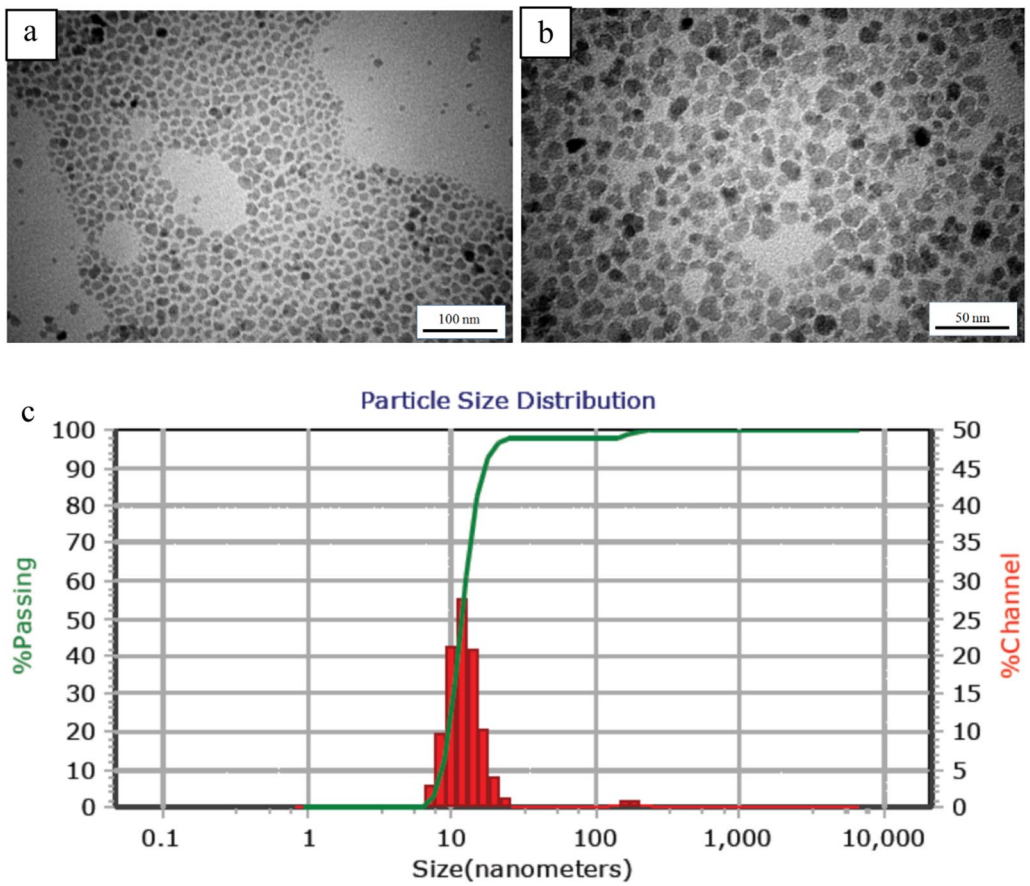

Fig. 2 **a**, **b** TEM images of magnetic nanoparticles: **a** 100 nm, **b** 50 nm; **c** The size distribution and the average size of the modified IONPs

can be attributed to the absorption of water molecules on the surface of the IONPs [46, 49].

TGA analysis was employed to ensure the surface modification of the IONPs with oleic acid. Figure 3c, d demonstrates the TGA and the corresponding derivative (dTGA) curves of the coated IONPs. The weight loss observed at temperatures below 150 °C was negligible, which is assigned to the evaporation of the adsorbed water. The weight loss in the second transition region (temperature range 210–280 °C) has occurred owing to the elimination of the free or physically adsorbed oleic acid molecules [50]. The other weight loss observed at 333 °C is associated with the degradation of the oleic acid covalently bound to the IONP surface [51].

Figure 3e illustrates the field-dependent magnetization (M–H) curves of the IONPs. Results revealed the reversible field-dependent magnetization curves with no hysteresis loops, coercivity and remanent magnetization, which demonstrates that the net magnetization of the IONPs is zero in the absence of EMF [52]. These results express the super-paramagnetic behavior of the synthesized IONPs with high saturation magnetization value of 48.97 emu/g [46].

Ag/IO nanocomposites evaluation

FE-SEM image

Figures 4 and 5 show the FE-SEM image, EDX, and the element maps of Ag and the IONPs in the synthesized nanocomposites. EDX analysis confirmed the presence of Ag and the IONPs throughout the nanocomposites. According to the FE-SEM and the element map images, spherical nanoparticles are distributed uniformly among the fibers without any agglomerations.

Figure 4a–d demonstrates the effect of four different concentrations of the AgNPs on the nanocomposites containing a fixed amount of the IONPs (10%). In Fig. 4a, C, O, and Fe elements can be identified in the maps. When silver nitrate was added to the composite, Ag also appeared in the results. Additionally, as shown in the element maps of Fig. 4a–d, higher concentrations of silver nitrate in the prepared solution leads to the increased content of AgNPs in the nanocomposite structure. The

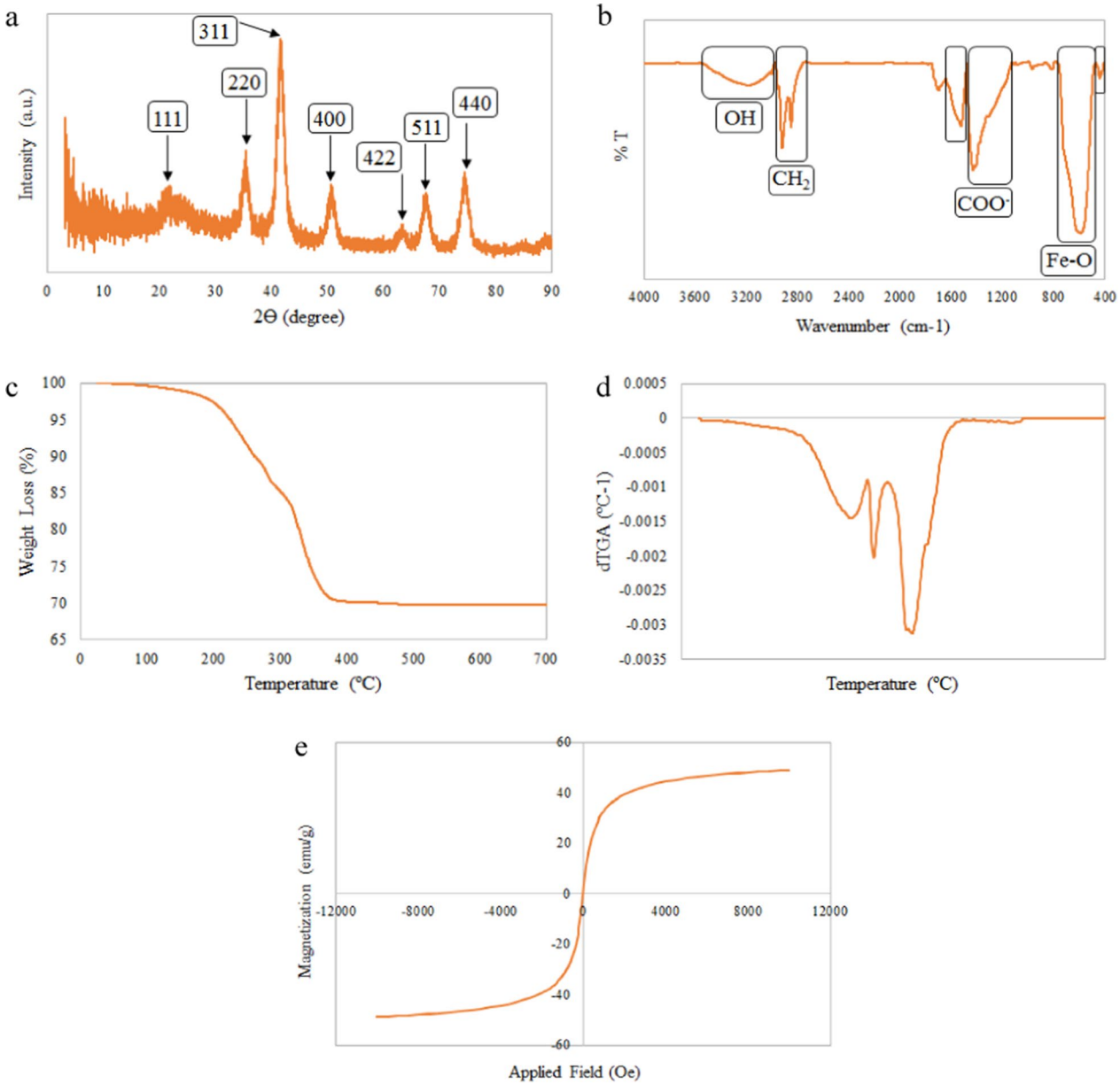

Fig. 3 **a** XRD pattern; **b** FTIR spectrum; **c** TGA curve and **b** dTGA curve; **e** Magnetization properties of the IONPs

constant intensity of Fe peaks in EDX analysis, as well as the good distribution of this element in the maps (a-d), indicates uniform coating of the IONPs in samples 9, 10, 11, and 12. The same trend exists in Fig. 5a–d. The small diversity of Ag density in the element maps shows the fixed amount of AgNPs in samples 3, 7, 11, and 15 synthesized using a constant concentration of the silver nitrate in the precursor solution. In proportion to the IONPs concentration in the coating solution, the IONPs content in the composites increases.

Crystalline structure

Figure 6a demonstrates the X-ray diffractograms of GA/PVA/PCL/Ag and GA/PVA/PCL/Ag/Fe_3O_4 nanocomposites. The addition of the IONPs to the nanocomposites has reduced the intensity of the peaks at 2θ = 24.95 & 27.69°, due to the interaction between PCL and the IONPs [53]. The IONP-containing nanocomposites showed three new peaks at 2θ = 34.82, 41.51 and 67.69° (for (220), (311), and (511) planes). Moreover, the intensity of the peaks increases at 2θ = 50.53 & 74.79° due to (400) and (440) planes, respectively.

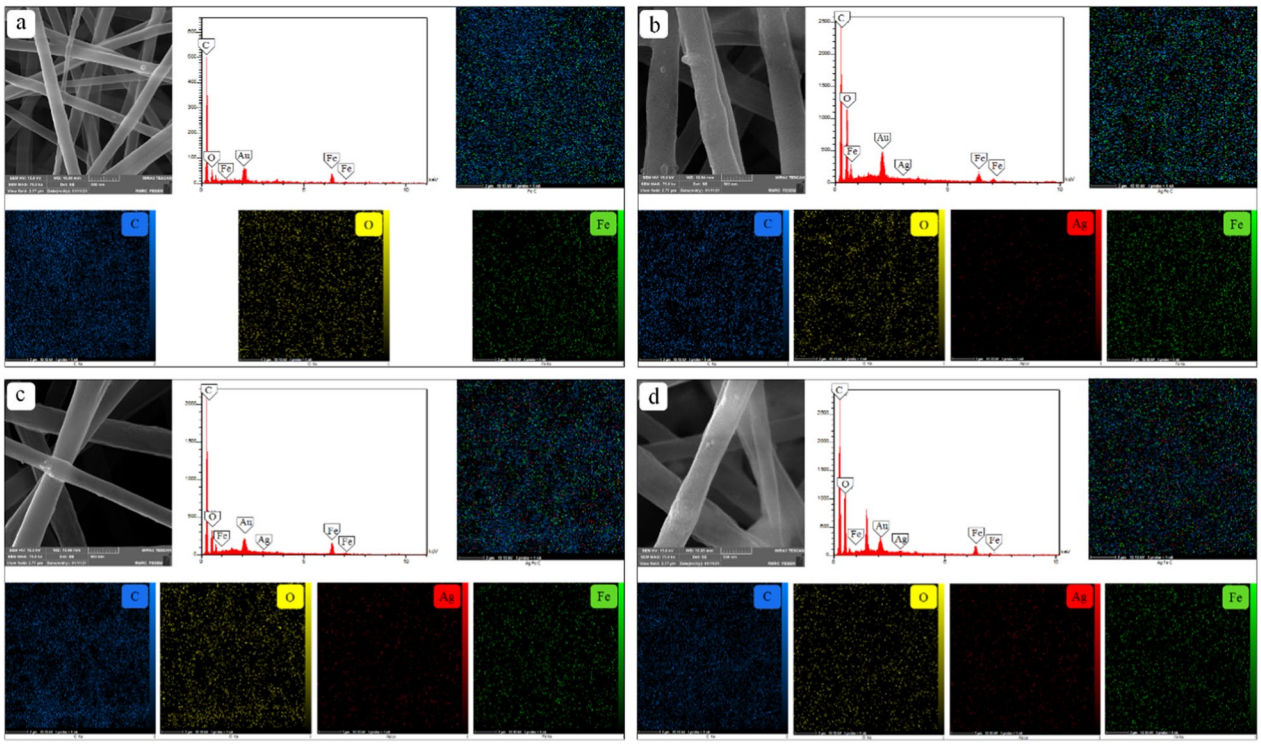

Fig. 4 FE-SEM images, EDX, and element maps of nanocomposites synthesized at the fixed IONPs concentration (10%) and different concentrations of AgNPs; **a** 0, **b** 0.05, **c** 0.5, **d** 1%

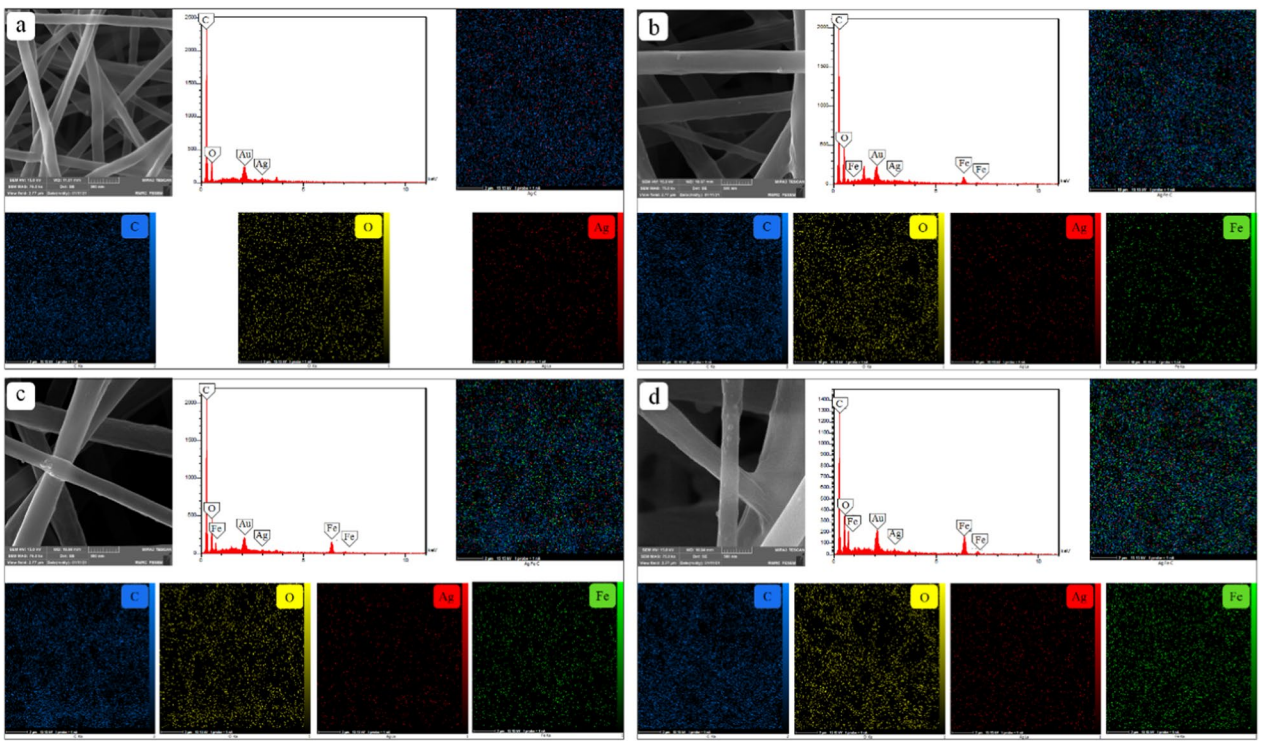

Fig. 5 FE-SEM images, EDX, and element maps of the nanocomposites synthesized at the fixed AgNPs concentration (0.5%) and different concentrations of IONPs; **a** 0, **b** 5, **c** 10, **d** 15%

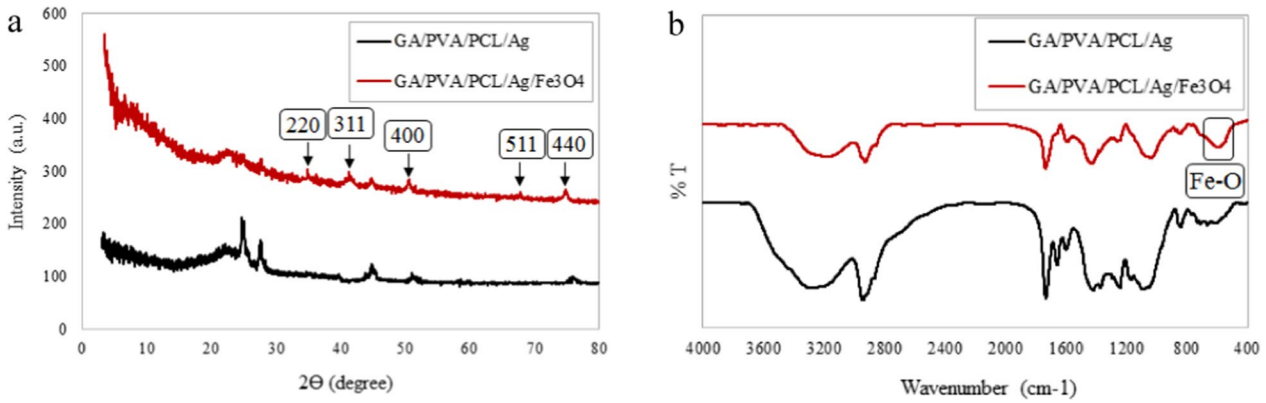

Fig. 6 **a** XRD pattern, and **b** FTIR spectra of GA/PVA/PCL/Ag and GA/PVA/PCL/Ag/IO nanocomposites

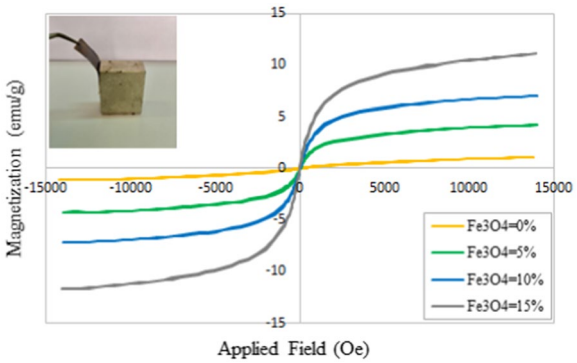

Fig. 7 The magnetization properties of the IONPs-containing nanocomposites

Chemical structure

FTIR spectra of GA/PVA/PCL/Ag and GA/PVA/PCL/Ag/Fe_3O_4 nanocomposites are shown in Fig. 6b. The main difference is the peak at 597 cm^{-1}. This peak is related to the stretching vibration of the metal–oxygen absorption band (Fe–O bond), indicative of the presence of the magnetite nanoparticles. Additionally, interactions between the IONPs and the nanocomposites can change the intensities or the peak shift. In the presence of the IONPs, the peaks of the hydroxyl group, C–H (asymmetric and stretching), C=O stretching vibration, COO^- symmetric stretching, and C–C stretching vibrations have been shifted to 3187, 2927, 1733, 1433, and 846 cm^{-1}, respectively [54].

Magnetic properties

The magnetization–magnetic field (M–H) curves of the nanocomposites at 300 K are shown in Fig. 7. The zero coercivity and the reversible hysteresis behavior of the nanocomposites reveal their super-paramagnetic property, which occurs only at the nanoscale. The saturation magnetization value of the IONPs was 48.97 emu/g, which was reduced to 4.23, 6.98, and 11.16 emu/g for the nanocomposites containing three different concentrations of the IONPs (5, 10, and 15%, respectively). However, the result also exhibits super-paramagnetic property [52, 55, 56]. Results demonstrate higher saturation magnetization values compared to the other researchers' studies such as Ahn and Kang [57]. Using the coating method instead of merging the nanoparticles into the solution prepared for the electrospinning process, increases the particle size and improves the magnetic property since magnetic characterization depends on the size of the synthesized nanoparticles [58].

Antibacterial activity

The effects of AgNPs content, IONPs concentration, and applying EMF, on the antibacterial activity of the nanocomposites against different microbial strains (*S. aureus* and *methicillin resistant Staphylococcus aureus (MRSA)* (Gram-positive), *P. aeruginosa* and *E. coli* (Gram-negative), and *C. albicans* (Yeast)), were investigated using two methods of disk diffusion and colony counting. Due to a large number of samples, only 5 samples include sample 1 (control sample), sample 4 (containing the highest amount of silver nanoparticles), sample 13 (containing the highest amount of iron oxide nanoparticles), sample 6 (containing the lowest amount of both silver nanoparticles and iron oxide) and Sample 16 (containing the highest amount of both silver nanoparticles and iron oxide) were used for microbial strains of *MRSA*, *E. coli*, and *C. albicans*.

According to Fig. 8a, b, the nanocomposites containing 0.05% AgNPs show low antibacterial activity. By increasing the concentration of AgNPs (to 1%), the diameter of the inhibition zone increases since more AgNPs can be released and higher antibacterial activity can be obtained (Figs. 9a, b, 10a, b, 11a, b) [59, 60]. AgNPs adhesion to

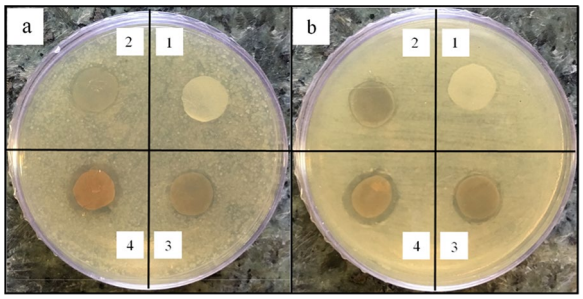

Fig. 8 Antibacterial activity of IONPs-free nanocomposites containing 0, 0.05, 0.5 and 1% AgNPs (samples 1, 2, 3 and 4, respectively) against **a** *Staphylococcus aureus*, and **b** *Pseudomonas aeruginosa*

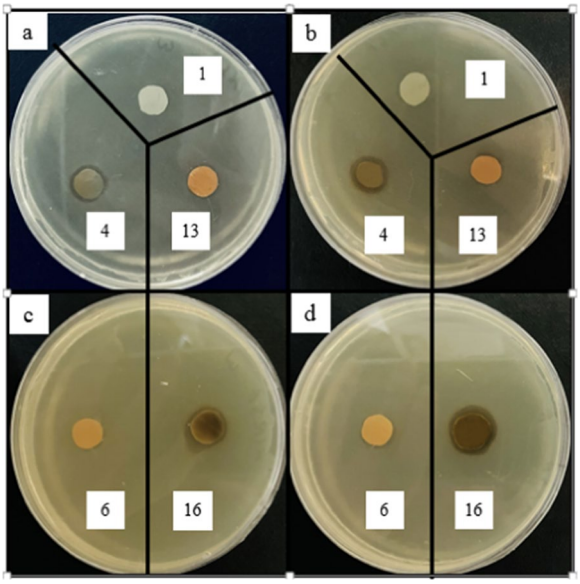

Fig. 9 Antibacterial activity of Ag/IO nanocomposites against *MRSA*, **a** and **c** in the absence and **b** and **d** in the presence of EMF

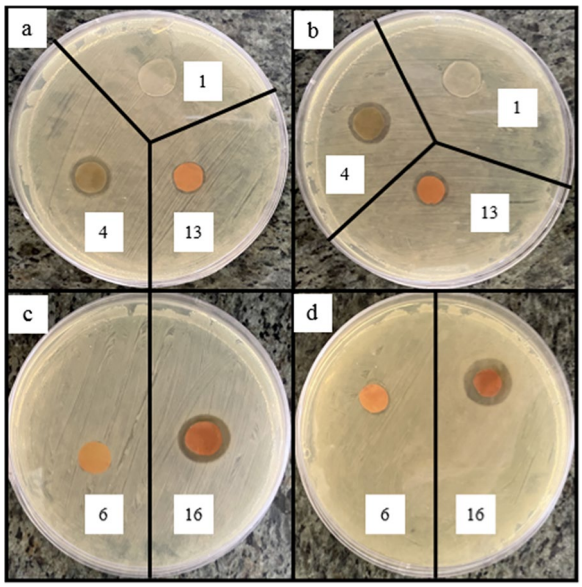

Fig. 10 Antibacterial activity of Ag/IO nanocomposites against *E.Coli*, **a** and **c** in the absence and **b** and **d** in the presence of EMF

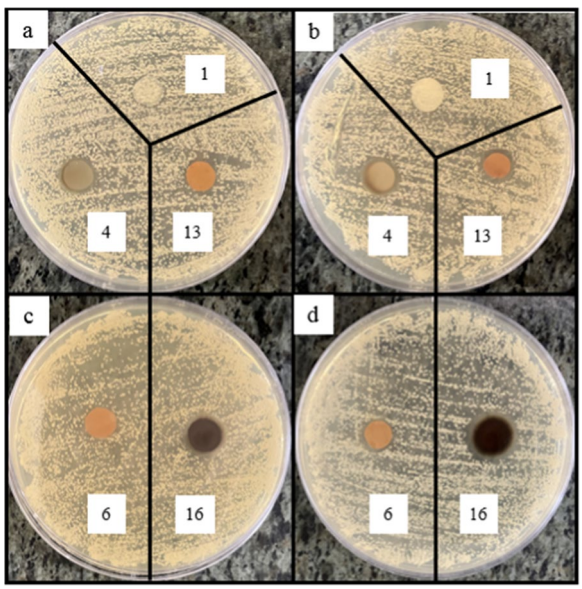

Fig. 11 Antibacterial activity of Ag/IO nanocomposites against *C. Albicans*, **a** and **c** in the absence and **b** and **d** in the presence of EMF

the cell wall through electrostatic interactions causes its damage. In the following, it penetrates the cell and pushes the cell content out, which results in DNA deformation and disrupting its transcription and translation, and the generation of reactive oxygen species (ROS) and free radicals [13, 61].

The content of IONPs in the nanocomposite is another influential factor affecting antibacterial activity. Figures 9a, b, 10a, b, 11a, b, 12a, b shows that increasing the IONPs content from 5 to 15% leads to increased antibacterial activity. The main mechanism of the antibacterial activity of IONPs is the oxidative stress caused by ROS. ROS involve superoxide radicals (O_2^-), hydroxyl radicals (–OH), singlet oxygen ($^1O_2$), and hydrogen peroxide (H_2O_2), which penetrate the bacteria cells and damage their proteins and DNA [62–64]. On the other hand, bacteria use adhesive surface structures to attach to tissues. The attachment of IONPs to the cell wall and surface structures of bacteria causes the bacterial adherence factors to be occupied and inactivated, preventing them from binding [65].

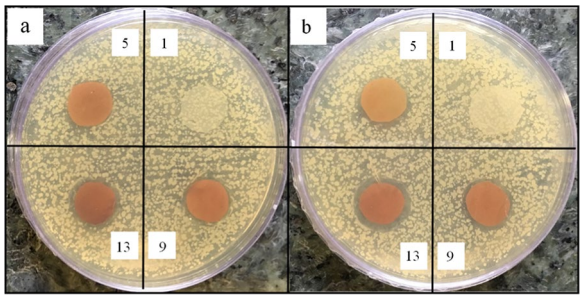

Fig. 12 Antibacterial test results of AgNPs-free nanocomposites containing 0, 5, 10 and 15% IONPs (samples 1, 5, 9, and 13, respectively) against *Staphylococcus aureus*, **a** in the absence and **b** in the presence of EMF

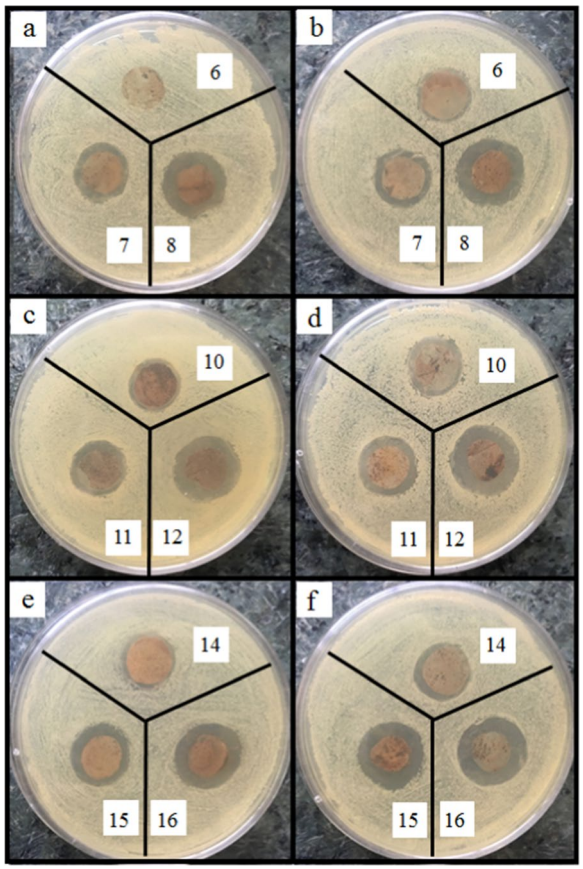

Fig. 13 Antibacterial activity of Ag/IO nanocomposites containing 0.05, 0.5, and 1% AgNPs; and 5% (**a** and **b**), 10% (**c** and **d**), and 15% IONPs (**e** and **f**) against *S. aureus*, (**a**, **c** and **e**) in the absence and (**b**, **d**, and **f**) in the presence of EMF

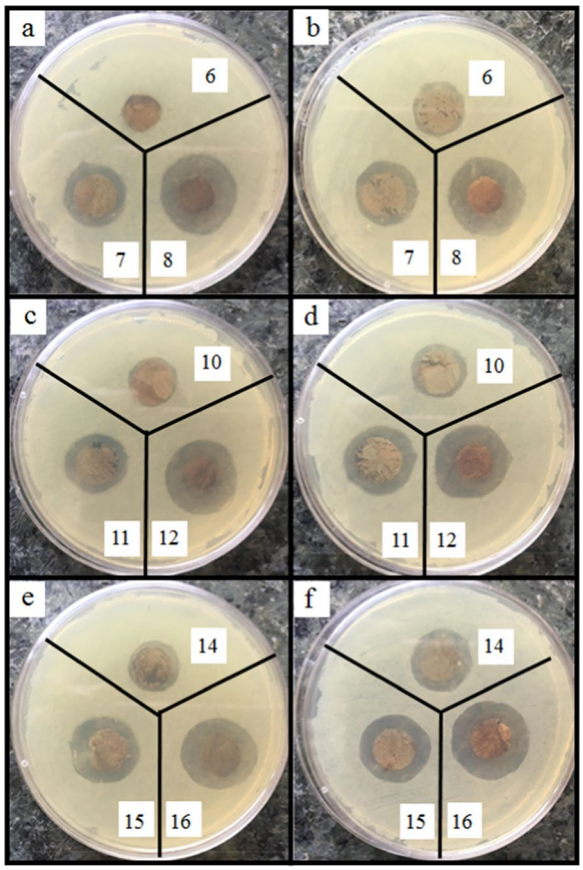

Fig. 14 Antibacterial activity of Ag/IO nanocomposites containing 0.05, 0.5, and 1% AgNPs; and 5% (**a** and **b**), 10% (**c** and **d**), and 15% IONPs (**e** and **f**) against *P. aeruginosa*, (**a**, **c** and **e**) in the absence and (**b**, **d**, and **f**) in the presence of EMF

A comparison of the images in Figs. 9c, d, 10c, d, 11c, d, 13, 14 and the data in Tables 1, 2, 3, 4 and 5 demonstrates that the presence of EMF increases the antibacterial activity of IONPs-containing nanocomposites. The magnetic moments of the IONPs are randomly oriented in the absence of EMF. Therefore, net magnetization is zero. Applying a strong enough EMF forces the magnetic moments of the IONPs to align along the magnetic field direction [66].

Due to the reasonable amount of the IONPs in the nanocomposites and their superparamagnetic properties, the applied EMF increases the IONPs release and improves the antibacterial activity. Moreover, the controlled release of IONPs leads to the more accessible release of the AgNPs, due to the increased porosity, and

Table 1 Inhibition zone diameter (mm) for *S. aureus*

IONPs concentration (%)	AgNPs concentration (%)		
	0.05	0.5	1
5			
A EMF*	10 ± 0.06	11.8 ± 0.15	13 ± 0.06
P EMF**	11 ± 0.1	12.8 ± 0.06	14.1 ± 0.1
10			
A EMF*	11.5 ± 0.1	12 ± 0.12	13.5 ± 0.1
P EMF**	12.5 ± 0.15	13 ± 0.06	14.5 ± 0.1
15			
A EMF*	12 ± 0.15	12.9 ± 0.1	14 ± 0.06
P EMF**	12.5 ± 0.1	13.8 ± 0.1	15 ± 0.15

A EMF *: absence of external magnetic field

P EMF **: presence of external magnetic field

Table 2 Inhibition zone diameter (mm) for *P. aeruginosa*

IONPs concentration (%)	AgNPs concentration (%)		
	0.05	0.5	1
5			
A EMF*	10 ± 0.06	12.5 ± 0.15	15 ± 0.15
P EMF**	11.2 ± 0.21	13.1 ± 0.15	16 ± 0.06
10			
A EMF*	10.5 ± 0.1	13 ± 0.06	15.5 ± 0.1
P EMF**	11.6 ± 0.06	14.2 ± 0.1	16.5 ± 0.06
15			
A EMF*	11 ± 0.15	13.7 ± 0.12	16 ± 0.1
P EMF**	12.4 ± 0.06	15.1 ± 0.15	16.8 ± 0.12

A EMF *: absence of external magnetic field

P EMF **: presence of external magnetic field

Table 3 Inhibition zone diameter (mm) for *MRSA*

IONPs concentration (%)	AgNPs concentration (%)			
	0	0.05	0.5	1
0	0	–	–	12.8 ± 0.06
5				
A EMF*	–	10 ± 0.06	–	–
P EMF**	–	10.8 ± 0.1	–	–
10				
A EMF*	–	–	–	–
P EMF**	–	–	–	–
15				
A EMF*	11 ± 0.15	–	–	14 ± 0.06
P EMF**	12 ± 0.1	–	–	14.9 ± 0.15

A EMF *: absence of external magnetic field

P EMF **: presence of external magnetic field

Table 4 Inhibition zone diameter (mm) for *E. Coli*

IONPs concentration (%)	AgNPs concentration (%)			
	0	0.05	0.5	1
0	0	–	–	13.6 ± 0.1
5				
A EMF*	–	10 ± 0.06	–	–
P EMF**	–	11 ± 0.15	–	–
10				
A EMF*	–	–	–	–
P EMF**	–	–	–	–
15				
A EMF*	12 ± 0.15	–	–	15 ± 0.06
P EMF**	13 ± 0.06	–	–	15.8 ± 0.1

A EMF *: absence of external magnetic field

P EMF **: presence of external magnetic field

thus the better antibacterial activity of the nanocomposites [67, 68].

In addition to the disc diffusion assay, the antibacterial activity of the nanocomposites against two bacterial strains of *S. aureus* and *P. aeruginosa* was also carried out through the colony counting method, which is shown in Table 6.

From this table it is obvious that the number of bacterial colonies of petri dishes corresponding to nanocomposites containing silver and iron oxide nanoparticles for both pathogenic bacteria is significantly lower than the control nanocomposite (sample 1). The results show that the addition of silver nanoparticles (sample 4), the addition of iron oxide nanoparticles (sample 13), the simultaneous integration of both nanoparticles (samples 6 and

Table 5 Inhibition zone diameter (mm) for *C. Albicans*

IONPs concentration (%)	AgNPs concentration (%)			
	0	0.05	0.5	1
0	0	–	–	13.2 ± 0.06
5				
A EMF*	–	10 ± 0.06	–	–
P EMF**	–	11 ± 0.1	–	–
10				
A EMF*	–	–	–	–
P EMF**	–	–	–	–
15				
A EMF*	12 ± 0.15	–	–	14.2 ± 0.15
P EMF**	13 ± 0.1	–	–	15 ± 0.15

A EMF *: absence of external magnetic field

P EMF **: presence of external magnetic field

Table 6 Bacterial Growth Inhibition (%) of the nanocomposites against *S. aureus*, and *P. aeruginosa*

	Bacterial growth inhibition (%)			
Bacteria	4	6	13	16
	A EMF			
S. aureus	98.82	89.23	94.62	99.91
P. aeruginosa	98.92	90.00	95.74	99.92
	P EMF			
S. aureus	98.82	97.31	98.65	99.98
P. aeruginosa	98.92	98.33	98.83	99.99

A EMF *: absence of external magnetic field

P EMF **: presence of external magnetic field

13), and the use of a magnetic field reduce the number of bacterial colonies. These results are in agreement with agar disk diffusion analysis.

Among the microbial strains, *P.aeruginosa* and *MRSA* showed the highest and lowest sensitivity to the antibacterial nanocomposites, respectively. The observed differences can be attributed to the presence of a thick layer of peptidoglycan in the cell wall of gram-positive bacteria, which acts like a barrier against the penetration of the antibacterial nanoparticles into the bacteria and affects their performance [39, 69].

ROS generaion

ROS generation was measured by the DCFH-DA assay after exposing the nanocomposites to *S. aureus* and *P. aeruginosa* to ascertain whether it has an effect on the antibacterial mechanism of Ag/IO nanocomposites or not. The results revealed that NPs-containing nanocomposites, produced more ROS compared to untreated nanocomposite, in the presence of both *S. aureus* and *P. aeruginosa* in a concentration-dependent manner. Increasing the concentration of AgNPs to 1% leads to about 8% increase in ROS as compared to NPs-free nanocomposites. Similarly, bacteria exposed to IONPs-containing nanocomposites demonstrated increased ROS production (Fig. 15).

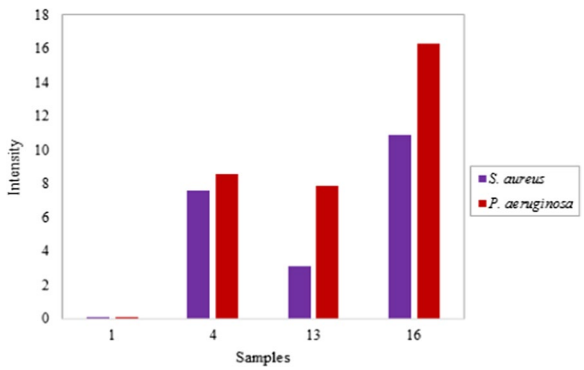

Fig. 15 Effect of Ag/IO NPs-containing nanocomposites on ROS formation in presence of *S. aureus* and *P. aeruginosa* bacterial cells

Altogether, the above data suggest that AgNPs act as oxidative stress inducer agents and cause the loss of cell viability in *S. aureus* and *P. aeruginosa* bacteria through ROS generation. ROS formation of AgNPs-containing nanocomposites can be assigned to the higher silver ion release. The interaction between metal NPs and bacterial cells often leads to ROS production, which damage to proteins and nucleic acids. The IONPs also produce ROS at their surface and increasing the concentration, causes increased ROS formation as more NPs are released from the nanocomposites [39, 70]. Taken together, the above finding suggest that ROS formation is a possible mechanism responsible for bacterial cell death in presence of Ag/IO nanocomposites.

Cytotoxicity

Cytotoxicity assay was carried out to study the biocompatibility of AgNPs, IONPs, and EMF on the fibroblast and macrophage cells. Cells were cultured on the nanocomposites for 1, 3, 5, and 7 days to perform the MTT assay. Generally, the type of nanoparticles, their shape, size, dose, surface properties, and the ways they are added to the system affect their toxicity [58]. According to Figs. 16a, b and 17, cells were able to grow on all nanocomposites; but increasing AgNPs and IONPs contents in the nanocomposites reduced cell proliferation due to the more released silver and iron oxide nanoparticles. Results revealed dose-dependent cytotoxicity of the silver nanoparticles [4, 16]. Increasing the AgNPs concentration to 1% reduced cell viability of fibroblasts and macrophages to about 80%. Ankamwar et al. showed that IONPs are not toxic in the concentration range of 0.1–10 $\mu g/mL^{-1}$, but cell viability decreases when the concentration reaches 100 $\mu g/mL^{-1}$ [71] and our study is in agreement with the mentioned report. Increasing the concentration of IONPs from 5 to 15% on the first day, caused a decrease in fibroblast viability from 83.1 to 77.8%. A low concentration of IONPs caused no toxicity in macrophages, even slight growth promotion is observed in prior research [72]. At the concentration of 15% IONPs phagocytic cells exhibited a higher survival rate of 85.1% [73]. According to previous reports, higher concentrations of IONPs could exert cytotoxicity by the generation of excessive reactive oxygen species (ROS). Additionally, IONPs impair cellular activities and cell growth by adsorbing proteins and other nutrients of the cell culture medium [72, 74].

Figures 16c and 17 shows the simultaneous effect of AgNPs and IONPs on the biocompatibility of the

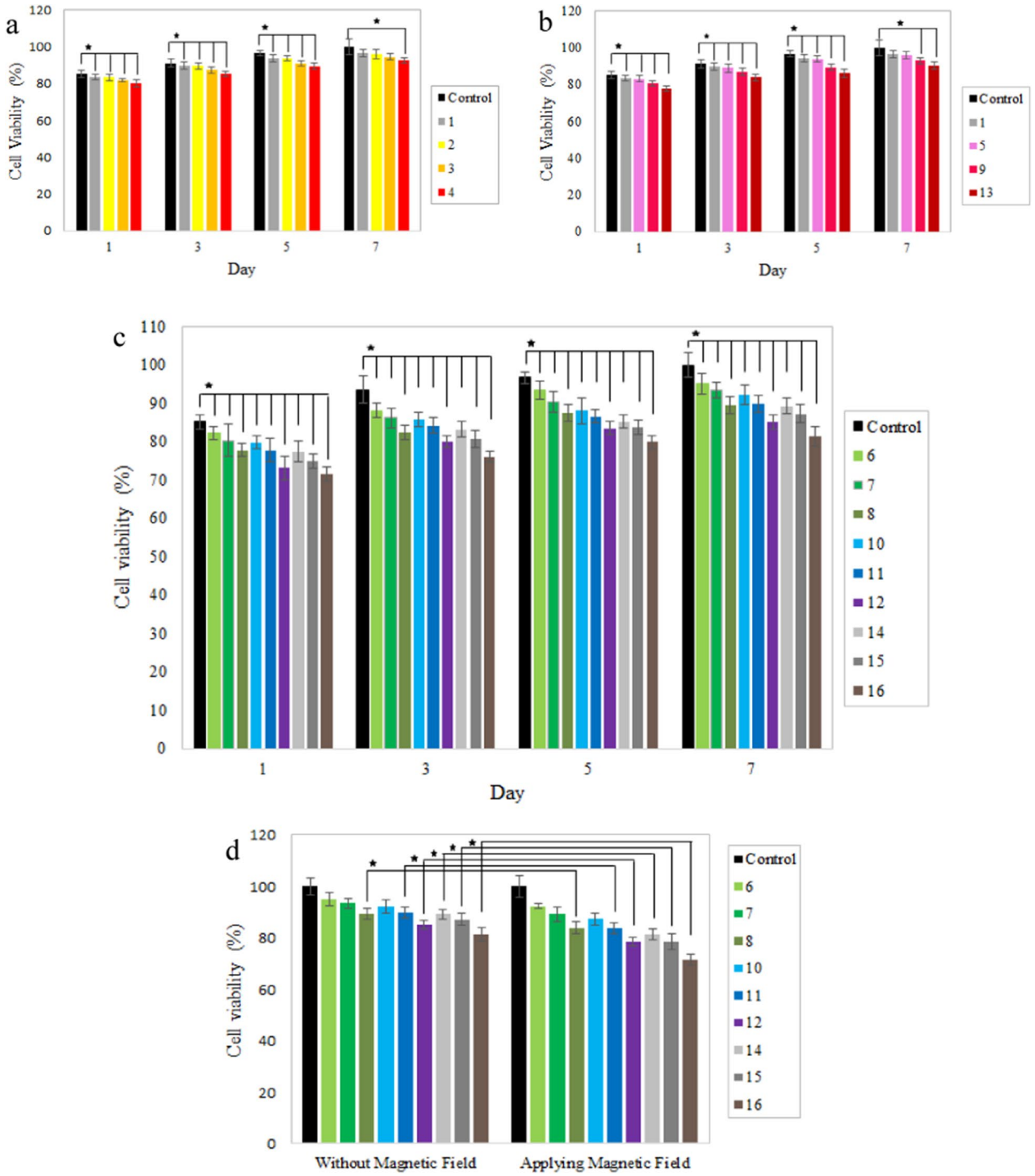

Fig. 16 MTT assay results of the **a** IONPs-free nanocomposites containing 0, 0.05, 0.5, and 1% AgNPs; **b** AgNPs-free nanocomposites containing 0, 5, 10, and 15% IONPs; **c** Ag/IO nanocomposites containing 0.05, 0.5, and 1% AgNPs; and 5, 10, and 15% IONPs on days 1, 3, 5 and 7; **d** Ag/IO nanocomposites containing 0.05, 0.5, and 1% AgNPs; and 5, 10, and 15% IONPs on the 7th day in the absence and presence of EMF. Data are reported as mean ± SD (n = 5 and *p < 0.05)

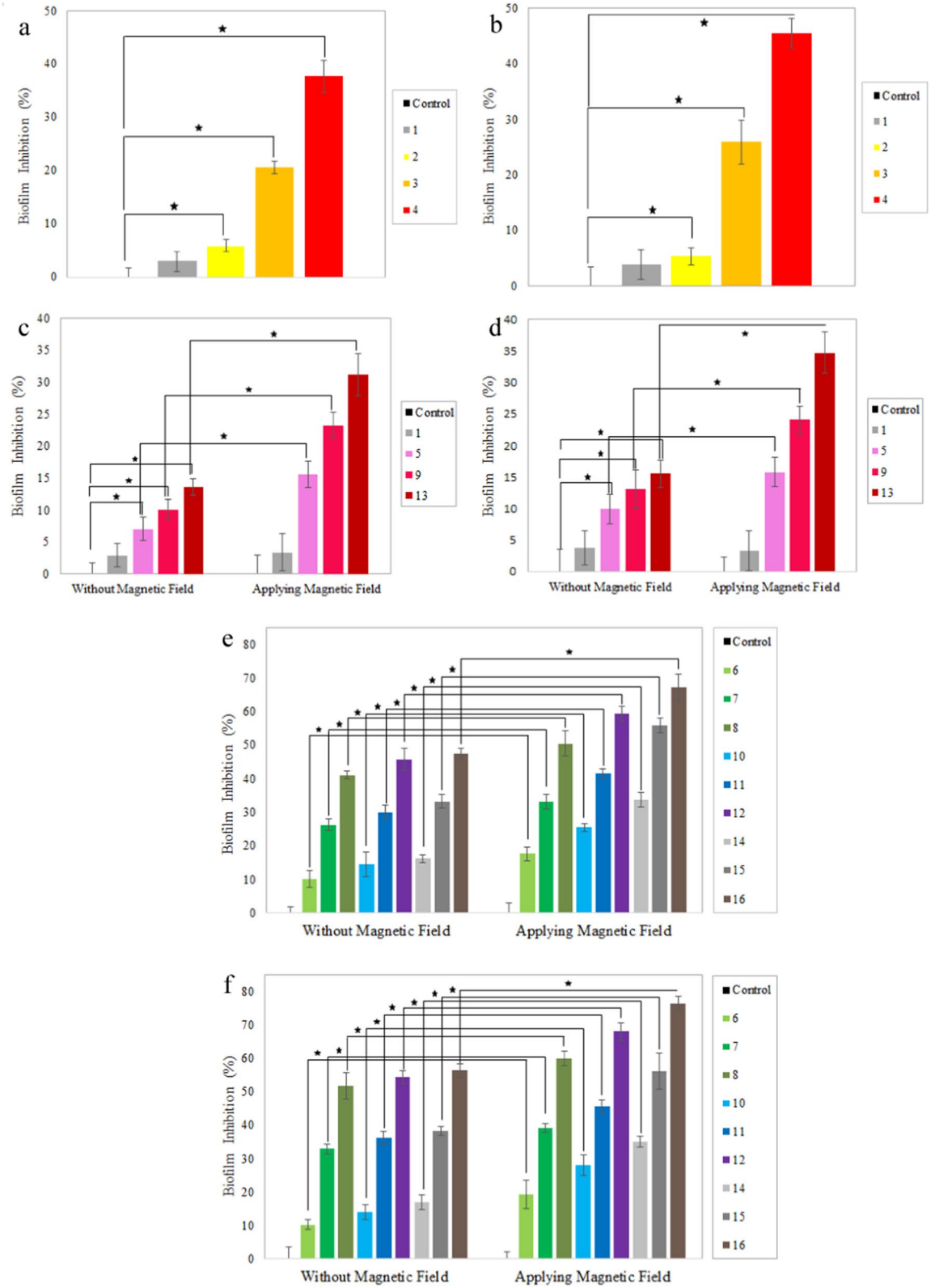

Fig. 17 Cell viability (%) of macrophage cells at different time incubation

nanocomposites. As presented in these figure, when both NPs are integrated into the nanocomposite, their cytotoxicity increases. Moreover, the nanocomposites containing high concentrations of AgNPs and IONPs on days 1 and 3 showed higher levels of toxicity, and the cell viability reduced to less than 80% for both cell types. However, cell viability was improved even for the nanocomposites containing the maximum amounts of the nanoparticles (sample 16) because of the considerable increase in the cell proliferation from day 5. Therefore, the incorporation of AgNPs and IONPs does not considerably affect the biocompatibility of the nanocomposites.

According to Fig. 16d, applying an EMF to the nanocomposites with a low concentration of the nanoparticles has no considerable effect on the cell viability, but the nanocomposites containing 15% IONPs release more IONPs and AgNPs and consequently increase the system's cytotoxicity [75].

Generally, due to the larger size of eukaryotic cells than prokaryotes and their structural differences, higher concentrations of nanoparticles are required to cause cytotoxicity in them. Using nanoparticles in low concentrations that are effective against microorganisms, has no toxic effect on the eukaryotic cells [76].

Antibiofilm activity

More than 60% of bacterial infections are caused by the formation of biofilms in chronic wounds. Unlike planktonic bacteria, which are easily killed, biofilms attach to the surface and are resistant to multiple antibiotics, which makes their inhibition difficult. Therefore, in this study, the inhibitory effect of Ag/IO nanocomposites against *S.aureus* and *P.aeruginosa* biofilms was investigated through a crystal violet staining assay.

According to Fig. 18a, b, the nanoparticles-free nanocomposites (sample 1) have no significant effect on the biofilm inhibition, but the addition of small amounts of AgNPs (0.05%) to the nanocomposites, resulted in 6 and 5% biofilm inhibition by *S.aureus* and *P.aeruginosa*, respectively; while AgNPs content increases up to 1%, promotes the biofilm inhibition to 38 and 45%, respectively [16, 77, 78].

Figure 18c, d shows the effect of different concentrations of IONPs on biofilm inhibition. The nanocomposites containing 5, 10, and 15% IONPs inhibit 7, 10, and 14% of *S. aureus* biofilm, respectively. The same trend was observed for *P. aeruginosa*, and with an increase in IONPs content from 5 to 10% and 15%, biofilm inhibition boosts from 10 to 13% and 15%, respectively [79]. There are several mechanisms of biofilm inhibition and antibacterial activity of IONPs, one of which is the generation of ROS. In addition, the electrostatic interactions between the nanoparticles and the bacterial cell wall leading to its destruction and bacterial death [62].

As presented in Fig. 18e, f, the biofilm inhibition increments with increasing silver and iron oxide nanoparticles. A comparison of the results shows that an increase of 0.5% in the amount of AgNPs has a more remarkable effect than an increase of 5% in the amount of IONPs.

A comparison of the nanocomposites manifests that applying EMF significantly enhances the inhibitory effect

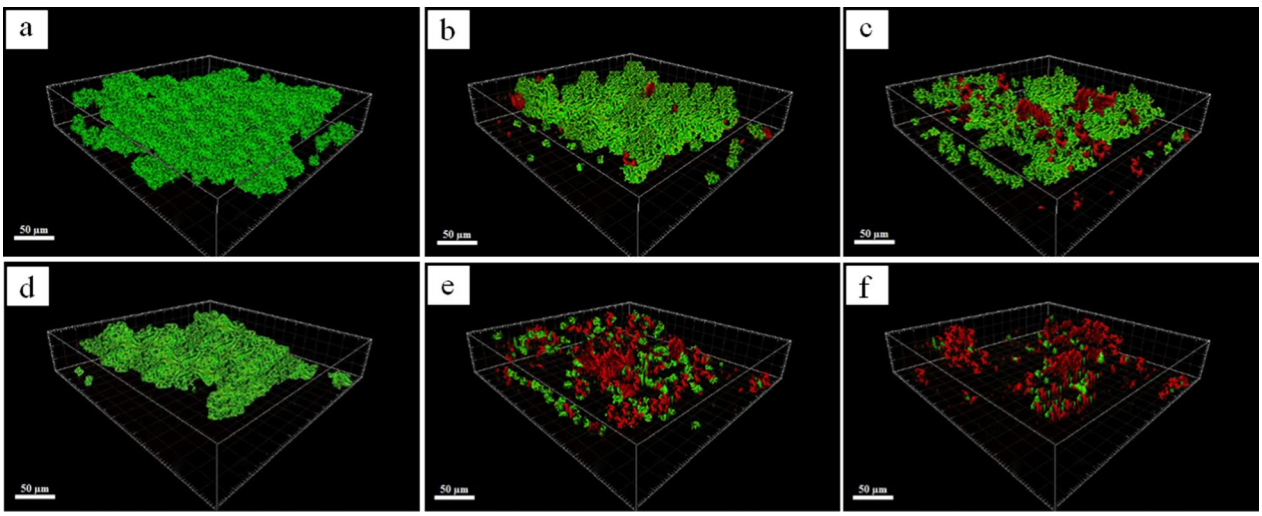

Fig. 18 Antibiofilm analysis of **a**, **b** IONPs-free nanocomposites containing 0, 0.05, 0.5, and 1% AgNPs (samples 1, 2, 3, and 4) against **a** *S. aureus*, and **b** *P. aeruginosa*; **c**, **d** AgNPs-free nanocomposites containing 0, 5, 10, and 15% IONPs (samples 1, 5, 9 and 13) in the absence and presence of EMF against **c** *S. aureus*, and **d** *P. aeruginosa*; **e**, **f** Ag/IO nanocomposites containing 0.05, 0.5, and 1% AgNPs; and 5, 10, and 15% IONPs in the absence and presence EMF against **e** *S. aureus*, and **f** *P. aeruginosa*. Data are reported as the mean ± SD (n = 5 and *p < 0.05)

due to the increased release of IONPs and consequently AgNPs. As a result, more AgNPs penetrate the biofilm, leading to further inhibition. In addition to the antibacterial properties, IONPs in the presence of EMF can mechanically destroy the biofilm structure by penetrating it and showing more inhibitory effects. Additionally, in the presence of EMF, iron oxide nanoparticles can be more permeable into the bacterial cell wall by converting the magnetic energy into heat [80]. The highest inhibitory activity of the nanocomposites against the biofilm of *S. aureus* and *P. aeruginosa* was in sample 16, increased significantly upon applying EMF.

Visual observation of the effects of the nanocomposite and EMF application on biofilm inhibition was obtained using CLSM images (Fig. 19). Samples 6 and 16 were selected for biofilm inhibition of *S. aurous* and *P. aeruginosa*, respectively. The cells were stained with SYTO9 (green) for living cells and propidium iodide (red) for dead cells.

As shown in Fig. 19a, *S. aureus* bacteria adhere to the surface, enclosed in the extracellular polymeric substance, and form a dense and thick biofilm. After treatment of biofilm with sample 6, some of the bacteria are killed (Fig. 19b). In fact, AgNPs and IONPs, with a high surface-to-volume ratio, were released, dispersed, and bound to the bacteria, and damaged their wall, but the biofilm still existed and retained its overall matrix. By applying EMF, the diffusivity of the nanoparticles into the biofilm was increased, which led to a decrease in the biofilm density. A comparison of images (b) and (c) reveals that although the structure of sample 6 could not kill the bacteria of the biofilm effectively, nanoparticles inhibited the bacterial adhesion and suppressed EPS synthesis [9]. A similar trend was also observed for inhibition of *P. aeruginosa* biofilm. However, Ag/IO nanocomposites had a significant effect on *P. aeruginosa* biofilm compared to *S. aureus*. Figure 19d–f demonstrates that after treatment of biofilm with sample 16, the matrix is damaged and only some clusters of bacterial cells are retained. Furthermore, when the biofilm is exposed to EMF, more than 90% of the biofilm is eradicated and only a few bacterial microcolonies are survived. CLSM results are consistent with the results obtained from the crystal violet staining method.

Based on the outcome, it can be concluded that although silver is a strong antibacterial material, it has low diffusivity in biofilm. According to the scientific reports, using high concentrations of silver nanoparticles for further biofilm inhibition could not be considered an effective method due to the agglomeration and increase in the size of the nanoparticles. This fact is evident in the studies performed by Alharbi et al. (0.5%) [42], Cochis et al. (1.7–1.9%) [81], and Grumezescu et al. (1 mg/cm^2) [82], that have used the same or even higher nanoparticle concentrations than the present study. On the other hand, the addition of IONPs to AgNPs and using EMF make the silver nanoparticles more functional and improve their efficiency for biofilm inhibition.

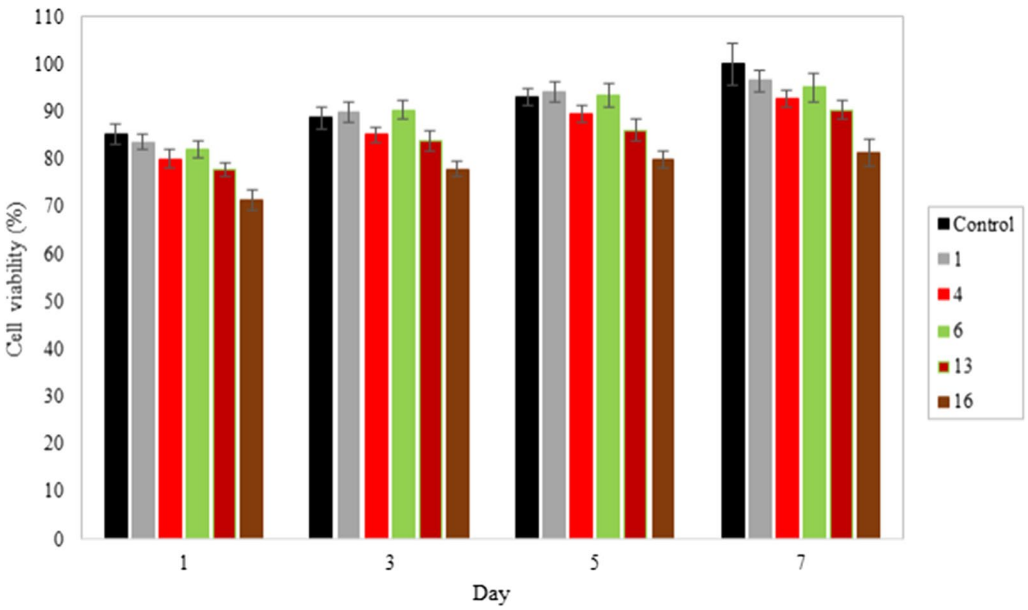

Fig. 19 CLSM analysis of the biofilms formed by *S. aureus* (**a**, **b**, and **c**) and *P. aeruginosa* (**d**, **e**, and **f**), Control (**a** and **d**), nanocomposite in the absence of EMF (b and e), nanocomposite in the presence of EMF (**c** and **f**)

Conclusion

In this research, various concentrations of AgNPs and IONPs were used in providing nanocomposites to evaluate their influence on the treatment of infected wounds. The results demonstrated that the use of IONPs can improve the effectiveness of the nanocomposites' antibacterial properties in such a way that the intended purpose was achieved without having to use high concentrations or doses of AgNPs, which are the main cause of the wound dressing's toxicity. Furthermore, EMF can have a superior effect on the release of the IONPs which can be followed by a remarkable release of the AgNPs, resulting in noticeable inhibition in biofilm formation to about 40%.

Abbreviations

AgNPs	Silver nanoparticles
CLSM	Confocal laser scanning microscopy
DLS	Dynamic light scattering
DMEM	Dulbecco's modified Eagle's medium
DMF	Dimethylformamide
DMSO	Dimethyl sulfoxide
EDX	Energy-dispersive x-ray spectroscopy
ELISA	Enzyme-linked immunosorbent assay
EMF	External magnetic field
EPS	Extracellular polymeric substance
FBS	Fetal bovine serum
FE-SEM	Field emission- scanning electron microscopy
FTIR	Fourier-transform infrared spectroscopy
GA	Gum Arabic
IONPs	Iron oxide nanoparticles
MEF	Mouse embryonic fibroblast
MTT	3-(4,5-Dimethylthiazol-2-yl)2,5-diphenyltetrazolium bromide
OD	Optical density
PBS	Phosphate-buffered saline
PCL	Polycaprolacton
PI	Propidium iodide
PVA	Polyvinyl alcohol
TEM	Transmission electron microscopy
TGA	Thermogravimetric analysis
VSM	Vibrating-sample magnetometer
XRD	X-ray powder diffraction

Acknowledgements

Not applicable.

Author contributions

NE: Investigation, Formal analysis, Methodology, Resources, Writing—original draft. SASh: Supervision, Project administration, Writing—review & editing. SHN: Conceptualization, Validation, Project administration, Resources. All authors read and approved the final manuscript.

Funding

This study was also supported by Tarbiat Modares University (TMU).

Availability of data and materials

The data that support the findings of this study are included within the article.

Declarations

Ethics approval and consent to participate

Not applicable.

Consent for publication

The manuscript is not under consideration for publication elsewhere.

Competing interests

The authors declare that they have no competing interests.

Author details

[1]Biotechnology Department, Faculty of Chemical Engineering, Tarbiat Modares University, 14155-4838, Tehran, Iran. [2]Biomedical Engineering Department, Faculty of Chemical Engineering, Tarbiat Modares University, Tehran, Iran.

Received: 10 December 2022 Accepted: 19 April 2023
Published online: 21 May 2023

References

1. Yu K, Lu F, Li Q, Chen H, Lu B, Liu J, et al. In situ assembly of Ag nanoparticles (AgNPs) on porous silkworm cocoon-based would film: Enhanced antimicrobial and wound healing activity. Sci Rep. 2017;7:1–13. https://doi.org/10.1038/s41598-017-02270-6.
2. Maslova E, Eisaiankhongi L, Sjöberg F, McCarthy RR. Burns and biofilms: priority pathogens and in vivo models. npj Biofilms Microbiomes. 2021;7:1–9. https://doi.org/10.1038/s41522-021-00243-2.
3. Liu Z, Wang F, Ren J, Qu X. A series of MOF/Ce-based nanozymes with dual enzyme-like activity disrupting biofilms and hindering recolonization of bacteria. Biomaterials. 2019;208:21–31. https://doi.org/10.1016/j.biomaterials.2019.04.007.
4. Sayed MA, Abd TMA, Rahman E, Abdelsalam HK, Ali AM, Hamdy MM, et al. Attractive study of the antimicrobial, antiviral, and cytotoxic activity of novel synthesized silver chromite nanocomposites. BMC Chem. 2022. https://doi.org/10.1186/s13065-022-00832-y.
5. Homaeigohar S, Boccaccini AR. Antibacterial biohybrid nanofibers for wound dressings. Acta Biomater. 2021;107:25–49. https://doi.org/10.1016/j.actbio.2020.02.022.
6. Rodrigues GR, López-Abarrategui C, de la Serna Gómez I, Dias SC, Otero-González AJ, Franco OL. Antimicrobial magnetic nanoparticles based-therapies for controlling infectious diseases. Int J Pharm. 2019;555:356–67. https://doi.org/10.1016/j.ijpharm.2018.11.043.
7. Taglietti A, Arciola CR, D'Agostino A, Dacarro G, Montanaro L, Campoccia D, et al. Antibiofilm activity of a monolayer of silver nanoparticles anchored to an amino-silanized glass surface. Biomaterials. 2014;35:1779–88. https://doi.org/10.1016/j.biomaterials.2013.11.047.
8. Provenzani R, San-Martin-Galindo P, Hassan G, Legehar A, Kallio A, Xhaard H, et al. Multisubstituted pyrimidines effectively inhibit bacterial growth and biofilm formation of Staphylococcus aureus. Sci Rep. 2021;11:1–10. https://doi.org/10.1038/s41598-021-86852-5.
9. Wang M, Huang X, Zheng H, Tang Y, Zeng K, Shao L, et al. Nanomaterials applied in wound healing : mechanisms, limitations and perspectives. J Control Release J. 2021;337:236–47.
10. Liu Y, Li Y, Shi L. Controlled drug delivery systems in eradicating bacterial biofilm-associated infections. J Control Release. 2020. https://doi.org/10.1016/j.jconrel.2020.10.038.
11. Aksoy İ, Küçükkeçeci H, Sevgi F, Metin Ö, Hatay PI. Photothermal antibacterial and antibiofilm activity of black phosphorus/gold nanocomposites against pathogenic bacteria. ACS Appl Mater Interfaces. 2020;12:26822–31.
12. Jang J, Lee JM, Bin OhS, Choi Y, Jung HS, Choi J. Development of antibiofilm nanocomposites: Ag/Cu bimetallic nanoparticles synthesized on the surface of graphene oxide nanosheets. ACS Appl Mater Interfaces. 2020;12:35826–34.
13. Nanobiotechnol J, Liu M, Liu T, Chen X, Yang J, Deng J, et al. Nano—silver—incorporated biomimetic polydopamine coating on a thermoplastic polyurethane porous nanocomposite as an efficient antibacterial wound dressing. J Nanobiotechnol. 2018. https://doi.org/10.1186/s12951-018-0416-4.
14. Tavakolian M, Munguia-Lopez JG, Valiei A, Islam MS, Kinsella JM, Tufenkji N, et al. Highly Absorbent Antibacterial and Biofilm-Disrupting Hydrogels

from Cellulose for Wound Dressing Applications. ACS Appl Mater Interfaces. 2020;12:39991–40001.
15. Qiu W, Han H, Li M, Li N, Wang Q, Qin X, et al. Nanofibers reinforced injectable hydrogel with self-healing, antibacterial, and hemostatic properties for chronic wound healing. J Colloid Interface Sci. 2021;596:312–23.
16. Geissel FJ, Platania V, Gogos A, Herrmann IK, Belibasakis GN, Chatzinikolaidou M, et al. Antibiofilm activity of nanosilver coatings against *Staphylococcus aureus*. J Colloid Interface Sci. 2021. https://doi.org/10.1016/j.jcis.2021.11.038.
17. Ambrogi V, Pietrella D, Nocchetti M, Casagrande S, Moretti V, De Marco S, et al. Montmorillonite–chitosan–chlorhexidine composite films with antibiofilm activity and improved cytotoxicity for wound dressing. J Colloid Interface Sci. 2017;491:265–72. https://doi.org/10.1016/j.jcis.2016.12.058.
18. Pérez-Díaz M, Alvarado-Gomez E, Magaña-Aquino M, Sánchez-Sánchez R, Velasquillo C, Gonzalez C, et al. Anti-biofilm activity of chitosan gels formulated with silver nanoparticles and their cytotoxic effect on human fibroblasts. Mater Sci Eng C. 2016;60:317–23. https://doi.org/10.1016/j.msec.2015.11.036.
19. Cheng H, Shi Z, Yue K, Huang X, Xu Y, Gao C, et al. Acta biomaterialia sprayable hydrogel dressing accelerates wound healing with combined reactive oxygen species-scavenging and antibacterial abilities. Acta Biomater. 2021;124:219–32. https://doi.org/10.1016/j.actbio.2021.02.002.
20. Loo CY, Rohanizadeh R, Young PM, Traini D, Cavaliere R, Whitchurch CB, et al. Combination of silver nanoparticles and curcumin nanoparticles for enhanced anti-biofilm activities. J Agric Food Chem. 2016;64:2513–22.
21. Loo CY, Young PM, Cavaliere R, Whitchurch CB, Lee WH, Rohanizadeh R. Silver nanoparticles enhance Pseudomonas aeruginosa PAO1 biofilm detachment. Drug Dev Ind Pharm. 2014;40:719–29.
22. Yu N, Cai T, Sun Y, Jiang C, Xiong H, Li Y, et al. A novel antibacterial agent based on AgNPs and Fe3O4 loaded chitin microspheres with peroxidase-like activity for synergistic antibacterial activity and wound-healing. Int J Pharm. 2018;552:277–87. https://doi.org/10.1016/j.ijpharm.2018.10.002.
23. Haidari H, Bright R, Strudwick XL, Garg S, Vasilev K. Multifunctional ultrasmall AgNP hydrogel accelerates healing of S. aureus infected wounds. Acta Biomater. 2021. https://doi.org/10.1016/j.actbio.2021.04.007.
24. Santos FG, Bonkovoski LC, Garcia FP, Cellet TSP, Witt MA, Nakamura CV, et al. Antibacterial performance of a PCL-PDMAEMA blend nanofiber-based scaffold enhanced with immobilized silver nanoparticles. ACS Appl Mater Interfaces. 2017;9:9304–14.
25. Wang Y, Cai B, Ni D, Sun Y, Wang G, Jiang H. A novel antibacterial and antifouling nanocomposite coated endotracheal tube to prevent ventilator—associated pneumonia. J Nanobiotechnol. 2022. https://doi.org/10.1186/s12951-022-01323-x.
26. Fei X, Jia M, Du X, Yang Y, Zhang R, Shao Z, et al. Green synthesis of silk fibroin-silver nanoparticle composites with e ff ective antibacterial and bio fi lm-disrupting properties. Biomacromol. 2013;14:4483–8.
27. Ezra L, O'Dell ZJ, Hui J, Riley KR. Emerging investigator series: quantifying silver nanoparticle aggregation kinetics in real-time using particle impact voltammetry coupled with UV-vis spectroscopy. Environ Sci Nano. 2020;7:2509–21.
28. Wu J, Li F, Hu X, Lu J, Sun X, Gao J, et al. Responsive assembly of silver nanoclusters with a biofilm locally amplified bactericidal effect to enhance treatments against multi-drug-resistant bacterial infections. ACS Cent Sci. 2019;5:1366–76.
29. Haidari H, Bright R, Garg S, Vasilev K, Cowin AJ, Kopecki Z. Eradication of mature bacterial biofilms with concurrent improvement in chronic wound healing using silver nanoparticle hydrogel treatment. Biomedicines. 2021;9:1182.
30. Marková Z, Šišková K, Filip J, Šafářová K, Prucek R, Aleš Panáček MK, Zbořil R. Chitosan-based synthesis of magnetically-driven nanocomposites with biogenic magnetite core, controlled silver size, and high antimicrobial activity. Green Chem. 2012;14:2550.
31. Padil VVT, Senan C, Wacławek S, Černík M. Electrospun fibers based on Arabic, karaya and kondagogu gums. Int J Biol Macromol. 2016;91:299–309.
32. Eghbalifam N, Shojaosadati SA, Hashemi-Najafabadi S, Khorasani AC. Synthesis and characterization of antimicrobial wound dressing material based on silver nanoparticles loaded gum Arabic nanofibers. Int J Biol Macromol. 2020;155:119–30. https://doi.org/10.1016/j.ijbiomac.2020.03.194.
33. Ghaseminezhad SM, Shojaosadati SA, Meyer RL. Ag/Fe3O4 nanocomposites penetrate and eradicate S. aureus biofilm in an in vitro chronic wound model. Colloids Surfaces B Biointerfaces. 2018;163:192–200. https://doi.org/10.1016/j.colsurfb.2017.12.035.
34. Durmus NG, Webster TJ. Eradicating antibiotic-resistant biofi lms with silver- conjugated superparamagnetic iron oxide nanoparticles. Adv Healthc Mater. 2013;2:165–71.
35. Gallo-Cordova A, Ovejero JG, Pablo-Sainz-Ezquerra AM, Cuya J, Jeyadevan B, Veintemillas-Verdaguer S, et al. Unravelling an amine-regulated crystallization crossover to prove single/multicore effects on the biomedical and environmental catalytic activity of magnetic iron oxide colloids. J Colloid Interface Sci. 2022;608:1585–97. https://doi.org/10.1016/j.jcis.2021.10.111.
36. Gasmalla HB, Lu X, Shinger MI, Ni L, Chishti AN. Novel magnetically separable of for enhanced photocatalytic and antibacterial activity against *Staphylococcus aureus* (S. aureus). J Nanobiotechnol. 2019. https://doi.org/10.1186/s12951-019-0485-z.
37. Mohammad M, Ahmadpoor F, Shojaosadati SA. Mussel-inspired magnetic nanoflowers as an effective nanozyme and antimicrobial agent for biosensing and catalytic reduction of organic dyes. ACS Omega. 2020;5:18766–77.
38. Wang J, Du L, Fu Y, Jiang P, Wang X. ZnO nanoparticles inhibit the activity of Porphyromonas gingivalis and *Actinomyces naeslundii* and promote the mineralization of the cementum. BMC Oral Health BMC Oral Health. 2019;19:1–11.
39. Yuan YG, Peng QL, Gurunathan S. Effects of silver nanoparticles on multiple drug-resistant strains of *Staphylococcus aureus* and *Pseudomonas aeruginosa* from mastitis-infected goats: an alternative approach for antimicrobial therapy. Int J Mol Sci. 2017;18:569.
40. Zhang K, Bai X, Yuan Z, Cao X, Jiao X, Li Y, et al. Layered nanofiber sponge with an improved capacity for promoting blood coagulation and wound healing. Biomaterials. 2019;204:70–9. https://doi.org/10.1016/j.biomaterials.2019.03.008.
41. Ghorbani F, Nojehdehyan H, Zamanian A, Gholipourmalekabadi M, Mozafari M. Synthesis, physico-chemical characteristics and cellular behavior of poly (lactic-co-glycolic acid)/gelatin nanofibrous scaffolds for engineering soft connective tissues. Adv Mater Lett. 2016;7:163–9.
42. Alharbi HF, Luqman M, Tabrez KS. Antibiofilm activity of synthesized electrospun core-shell nanofiber composites of PLA and PVA with silver nanoparticles. Mater Res Express. 2018;5:1–14.
43. Maslakci NN, Ulusoy S, Oksuz AU. Investigation of the effects of plasma-treated chitosan electrospun fibers onto biofilm formation. Sensors Actuators B Chem. 2017;246:887–95. https://doi.org/10.1016/j.snb.2017.02.089.
44. Qin H, Cao H, Zhao Y, Zhu C, Cheng T, Wang Q, et al. In vitro and in vivo anti-biofilm effects of silver nanoparticles immobilized on titanium. Biomaterials. 2014;35:9114–25.
45. Mohammadi H, Nekobahr E, Akhtari J, Saeedi M, Akbari J, Fathi F. Synthesis and characterization of magnetite nanoparticles by co-precipitation method coated with biocompatible compounds and evaluation of in-vitro cytotoxicity. Toxicol Rep. 2021;8:331–6. https://doi.org/10.1016/j.toxrep.2021.01.012.
46. Joshi R, Singh BP, Ningthoujam RS. Confirmation of highly stable 10 nm sized Fe3O4 nanoparticle formation at room temperature and understanding of heat-generation under AC magnetic fields for potential application in hyperthermia. AIP Adv. 2020;10:1–8. https://doi.org/10.1063/5.0022446.
47. Bao S, Tu M, Huang H, Wang C, Chen Y, Sun B, et al. Heterogeneous iron oxide nanoparticles anchored on carbon nanotubes for high-performance lithium-ion storage and fenton-like oxidation. J Colloid Interface Sci. 2021;601:283–93. https://doi.org/10.1016/j.jcis.2021.05.137.
48. Zhang H, Xia JY, Pang XL, Zhao M, Wang BQ, Yang LL, et al. Magnetic nanoparticle-loaded electrospun polymeric nanofibers for tissue engineering. Mater Sci Eng C. 2017;73:537–43. https://doi.org/10.1016/j.msec.2016.12.116.
49. Imran M, Ansari AR, Shaik AH, Abdulaziz Hussain S, Khan A, et al. Ferrofluid synthesis using oleic acid coated Fe3O4 nanoparticles dispersed in mineral oil for heat transfer applications. Mater Res Express. 2018;5:1–8.
50. Lai CW, Low FW, Tai MF, Abdul Hamid SB. Iron oxide nanoparticles decorated oleic acid for high colloidal stability. Adv Polym Technol. 2018;37:1712–21.

51. Urian YA, Atoche-Medrano JJ, Quispe LT, León Félix L, Coaquira JAH. Study of the surface properties and particle-particle interactions in oleic acid-coated Fe3O4 nanoparticles. J Magn Magn Mater. 2021;525:167686. https://doi.org/10.1016/j.jmmm.2020.167686.
52. Guo R, Jiao T, Xing R, Chen Y, Guo W, Zhou J, et al. Hierarchical AuNPs-loaded Fe3O4/Polymers nanocomposites constructed by electrospinning with enhanced and magnetically recyclable catalytic capacities. Nanomaterials. 2017;7:1–16.
53. Khandanlou R, Ahmad MB, Shameli K, Saki E, Kalantari K. Studies on properties of rice straw/polymer nanocomposites based on polycaprolactone and Fe3O4 nanoparticles and evaluation of antibacterial activity. Int J Mol Sci. 2014;15:18466–83.
54. Bhakat D, Barik P, Bhattacharjee A. Electrical conductivity behavior of Gum Arabic biopolymer-Fe3O4 nanocomposites. J Phys Chem Solids. 2018;112:73–9. https://doi.org/10.1016/j.jpcs.2017.09.002.
55. Amarjargal A, Tijing LD, Park C, Im I. Controlled assembly of superparamagnetic iron oxide nanoparticles on electrospun PU nanofibrous membrane: a novel heat-generating substrate for magnetic hyperthermia application. Eur Polym J. 2013;49:3796–805. https://doi.org/10.1016/j.eurpolymj.2013.08.026.
56. Rajagukguk J, Simamora P, Saragih CS, Abdullah H, Gultom NS, Imaduddin A. Superparamagnetic behaviour and surface analysis of Fe3O4/PPY/CNT nanocomposites. J Nanomater. 2020;2020:6.
57. Ahn BW, Kang TJ. Preparation and characterization of magnetic nanofibers with iron oxide nanoparticles and poly (ethylene terephthalate). J Appl Polym Sci. 2012;125:1567–75.
58. Matos RJR, Chaparro CIP, Silva JC, Valente MA, Borges JP, Soares PIP. Electrospun composite cellulose acetate/iron oxide nanoparticles nonwoven membranes for magnetic hyperthermia applications. Carbohydr Polym. 2018;198:9–16. https://doi.org/10.1016/j.carbpol.2018.06.048.
59. Yang G, Yao Y, Wang C. Green synthesis of silver nanoparticles impregnated bacterial cellulose-alginate composite film with improved properties. Mater Lett. 2017;209:11–4. https://doi.org/10.1016/j.matlet.2017.07.097.
60. He H, Tao G, Wang Y, Cai R, Guo P, Chen L, et al. In situ green synthesis and characterization of sericin-silver nanoparticle composite with effective antibacterial activity and good biocompatibility. Mater Sci Eng C. 2017;80:509–16. https://doi.org/10.1016/j.msec.2017.06.015.
61. Urnukhsaikhan E, Bold B-E, Gunbileg A, Sukhbaatar N, Mishig-Ochir T. Antibacterial activity and characteristics of silver nanoparticles biosynthesized from *Carduus crispus*. Sci Rep. 2021;11:1–12. https://doi.org/10.1038/s41598-021-00520-2.
62. Thukkaram M, Sitaram S, Kannaiyan SK, Subbiahdoss G. Antibacterial efficacy of iron-oxide nanoparticles against biofilms on different biomaterial surfaces. Int J Biomater. 2014;2014:1–7.
63. Armijo LM, Wawrzyniec SJ, Kopciuch M, Brandt YI, Rivera AC, Withers NJ, et al. Antibacterial activity of iron oxide, iron nitride, and tobramycin conjugated nanoparticles against Pseudomonas aeruginosa biofilms. J Nanobiotechnol. 2020;18:1–27. https://doi.org/10.1186/s12951-020-0588-6.
64. Gao F, Li X, Zhang T, Ghosal A, Zhang G, Ming H. Iron nanoparticles augmented chemodynamic e ff ect by alternative magnetic fi eld for wound disinfection and healing. J Control Release. 2020;324:598–609. https://doi.org/10.1016/j.jconrel.2020.06.003.
65. Hajjaji A, Elabidi M, Trabelsi K, Assadi AA, Bessais B, Rtimi S. Bacterial adhesion and inactivation on Ag decorated TiO2-nanotubes under visible light: effect of the nanotubes geometry on the photocatalytic activity. Colloids Surfaces B Biointerfaces. 2018;170:92–8. https://doi.org/10.1016/j.colsurfb.2018.06.005.
66. Borin D. Targeted patterning of magnetic microparticles in a polymer composite. Philos Trans R Soc A Math Phys Eng Sci. 2020;378:20190256.
67. Li J, Nickel R, Wu J, Lin F, Van Lierop J, Liu S. A new tool to attack biofilms: driving magnetic iron-oxide nanoparticles to disrupt the matrix. Nanoscale. 2019;11:6905–15.
68. Ranmadugala D, Ebrahiminezhad A, Manley-Harris M, Ghasemi Y, Berenjian A. The effect of iron oxide nanoparticles on *Bacillus subtilis* biofilm, growth and viability. Process Biochem. 2017;62:231–40. https://doi.org/10.1016/j.procbio.2017.07.003.
69. Bardania H, Mahmoudi R, Bagheri H, Salehpour Z, Fouani MH, Darabian B, et al. Facile preparation of a novel biogenic silver-loaded nanofilm with intrinsic anti-bacterial and oxidant scavenging activities for wound healing. Sci Rep. 2020;10:1–14.
70. Sukumar UK, Gopinath P. Field-actuated antineoplastic potential of smart and versatile PEO-bPEI electrospun scaffold by multi-staged targeted co-delivery of magnetite nanoparticles and niclosamide-bPEI complexes. RSC Adv. 2016;6:46186–201.
71. Ankamwar B, Lai TC, Huang JH, Liu RS, Hsiao M, Chen CH, et al. Biocompatibility of Fe3O4 nanoparticles evaluated by in vitro cytotoxicity assays using normal, glia and breast cancer cells. Nanotechnology. 2010;21:075102.
72. Zhang L, Tan S, Liu Y, Xie H, Luo B, Wang J. In vitro inhibition of tumor growth by low-dose iron oxide nanoparticles activating macrophages. J Biomater Appl. 2019;33:935–45.
73. Feng Q, Liu Y, Huang J, Chen K, Huang J, Xiao K. Uptake, distribution, clearance, and toxicity of iron oxide nanoparticles with different sizes and coatings. Sci Rep. 2018;8:1–13. https://doi.org/10.1038/s41598-018-19628-z.
74. Asad SS, Yassen KMSNY. Cytotoxic effect of iron nanoparticles in vitro on some cell lines. Iraqi J Cancer Med Genet. 2018;10:71–7.
75. Wei H, Hu Y, Wang J, Gao X, Qian X, Tang M. Superparamagnetic iron oxide nanoparticles: cytotoxicity, metabolism, and cellular behavior in biomedicine applications. Int J Nanomed. 2021;16:6097–113.
76. Duan Y-Y, Jia J, Wang S-H, Yan W, Jin L, Wang ZY. Preparation of antimicrobial poly(«-caprolactone) electrospun nanofibers containing silver-loaded zirconium phosphate nanoparticles. J Appl Polym Sci. 2007;106:1208–14.
77. Mohanta YK, Biswas K, Jena SK, Hashem A, AbdAllah EF, Mohanta TK. Anti-biofilm and antibacterial activities of silver nanoparticles synthesized by the reducing activity of phytoconstituents present in the indian medicinal plants. Front Microbiol. 2020;11:1–15.
78. Salman M, Rizwana R, Khan H, Munir I, Hamayun M, Iqbal A, et al. Synergistic effect of silver nanoparticles and polymyxin B against biofilm produced by *Pseudomonas aeruginosa* isolates of pus samples in vitro. Artif Cells, Nanomedicine Biotechnol. 2019;47:2465–72. https://doi.org/10.1080/21691401.2019.1626864.
79. Vallet-Regí M, González B, Izquierdo-Barba I. Nanomaterials as promising alternative in the infection treatment. Int J Mol Sci. 2019;20:3806.
80. Yeh YC, Huang TH, Yang SC, Chen CC, Fang JY. Nano-based drug delivery or targeting to eradicate bacteria for infection mitigation: a review of recent advances. Front Chem. 2020;8:1–22.
81. Cochis A, Ferraris S, Sorrentino R, Azzimonti B, Novara C, Geobaldo F, et al. Silver-doped keratin nanofibers preserve a titanium surface from biofilm contamination and favor soft-tissue healing. J Mater Chem B. 2017;5:8366–77.
82. Grumezescu AM, Stoica AE, Dima-Bălcescu MȘ, Chircov C, Gharbia S, Baltă C, et al. Electrospun polyethylene terephthalate nanofibers loaded with silver nanoparticles: novel approach in anti-infective therapy. J Clin Med. 2019;8:1–21.

Publisher's Note